Supplemental material to this article can be found at:
http://molpharm.aspetjournals.org/content/suppl/2024/01/09/molpharm.123.000789.DC1
1521-0111/105/3/233–249$35.00
MOLECULAR PHARMACOLOGY
dx.doi.org/10.1124/molpharm.123.000789
Mol Pharmacol 105:233–249, March 2024

Pharmacologic Characterization of LTGO-33, a Selective Small Molecule Inhibitor of the Voltage-Gated Sodium Channel $Na_V1.8$ with a Unique Mechanism of Action[S]

John M. Gilchrist, Nien-Du Yang, Victoria Jiang, and Bryan D. Moyer
Latigo Biotherapeutics, Inc., Thousand Oaks, California

Received September 26, 2023; accepted January 2, 2024

ABSTRACT

Discovery and development of new molecules directed against validated pain targets is required to advance the treatment of pain disorders. Voltage-gated sodium channels (Na_Vs) are responsible for action potential initiation and transmission of pain signals. $Na_V1.8$ is specifically expressed in peripheral nociceptors and has been genetically and pharmacologically validated as a human pain target. Selective inhibition of $Na_V1.8$ can ameliorate pain while minimizing effects on other Na_V isoforms essential for cardiac, respiratory, and central nervous system physiology. Here we present the pharmacology, interaction site, and mechanism of action of LTGO-33, a novel $Na_V1.8$ small molecule inhibitor. LTGO-33 inhibited $Na_V1.8$ in the nM potency range and exhibited over 600-fold selectivity against human $Na_V1.1$–$Na_V1.7$ and $Na_V1.9$. Unlike prior reported $Na_V1.8$ inhibitors that preferentially interacted with an inactivated state via the pore region, LTGO-33 was state-independent with similar potencies against closed and inactivated channels. LTGO-33 displayed species specificity for primate $Na_V1.8$ over dog and rodent $Na_V1.8$ and inhibited action potential firing in human dorsal root ganglia neurons. Using chimeras combined with mutagenesis, the extracellular cleft of the second voltage-sensing domain was identified as the key site required for channel inhibition. Biophysical mechanism of action studies demonstrated that LTGO-33 inhibition was relieved by membrane depolarization, suggesting the molecule stabilized the deactivated state to prevent channel opening. LTGO-33 equally inhibited wild-type and multiple $Na_V1.8$ variants associated with human pain disorders. These collective results illustrate LTGO-33 inhibition via both a novel interaction site and mechanism of action previously undescribed in $Na_V1.8$ small molecule pharmacologic space.

SIGNIFICANCE STATEMENT

$Na_V1.8$ sodium channels primarily expressed in peripheral pain-sensing neurons represent a validated target for the development of novel analgesics. Here we present the selective small molecule $Na_V1.8$ inhibitor LTGO-33 that interdicts a distinct site in a voltage-sensor domain to inhibit channel opening. These results inform the development of new analgesics for pain disorders.

Introduction

Pain represents a common reason patients seek medical care with over 30% of Americans reporting pain over a 3-month period and 11% suffering from daily chronic pain associated with worse health status and more disability (Mäntyselkä et al., 2001; Nahin, 2015; Lucas et al., 2021). Chronic pain, defined as persisting or reoccurring for 3 or more months, represents a significant unmet medical need impacting over 100 million Americans per year with an annual economic impact over $500 billion, exceeding heart disease, cancer, and diabetes (Treede et al., 2015; Holmes, 2016). Current pain therapies comprising NSAIDs, antidepressants, antiepileptics, and opioids suffer from limited efficacy, significant risk of abuse or dependence, and/or low tolerability with numbers needed to treat for one individual to achieve 50% or greater pain relief between 4 and 10 (Finnerup et al., 2015). The discontinuation of numerous molecules from clinical development coupled with the last approval of a new pain therapy more than 10 years ago highlights the pressing need to discover and develop new molecules against validated targets for the treatment of pain disorders (Knezevic et al., 2015).

Voltage-gated sodium channels, or Na_V channels, control the excitability of neurons in the peripheral (PNS) and central nervous system (Catterall, 2000). From a closed state, sodium channels open briefly upon membrane depolarization to let sodium ions into the cell and then rapidly inactivate to prevent sustained sodium influx (Ahern et al., 2016). Sodium currents entering pain sensing nociceptor neurons through Na_V channels drive the upstroke of an action potential (AP), the electrical means of sensory information transfer in the nervous system. In the PNS, sensory neurons in the dorsal root ganglia (DRG) are responsible for pain signaling. Action potentials are transmitted along peripheral afferent nerve fiber axons to the spinal

No specific funding was received for this work. This work was fully supported by Latigo Biotherapeutics, Inc.
All authors were employees of Latigo Biotherapeutics, Inc. at the time of publication.
dx.doi.org/10.1124/molpharm.123.000789.
[S] This article has supplemental material available at molpharm.aspetjournals.org.

ABBREVIATIONS: AP, action potential; DMEM, Dulbecco's modified Eagle's medium; DRG, dorsal root ganglia; $hNa_V1.8$, human $Na_V1.8$; Na_V, voltage-gated sodium channel; NEAA, non-essential amino acids; PNS, peripheral nervous system; $rNa_V1.8$, rat $Na_V1.8$; TTX, tetrodotoxin; TTX-R, tetrodotoxin-resistant; TTX-S, tetrodotoxin-sensitive; VSD, voltage-sensing domain; WT, wild-type.

cord and then to the central nervous system for pain signal processing and integration (Basbaum et al., 2009).

$Na_V1.8$ is a member of the voltage-gated sodium channel family specifically expressed in DRG neurons in the PNS (Han et al., 2016; Bennett et al., 2019; Shiers et al., 2020). The biophysical properties of $Na_V1.8$, specifically the right-shifted voltage-dependence of inactivation coupled with rapid recovery from inactivation, support $Na_V1.8$-mediated high frequency action potential firing in DRG neurons (Han et al., 2015). $Na_V1.8$ is a genetically and pharmacologically validated pain target in humans. Rare gain of function mutations in SCN10A, the gene encoding $Na_V1.8$ protein, are associated with or drive pain phenotypes in small fiber neuropathy, diabetic peripheral neuropathy, and trigeminal neuralgia (Faber et al., 2012; Huang et al., 2013; Han et al., 2014, 2018; Stefano et al., 2020). In contrast, a more common single nucleotide polymorphism is linked to reduced pain in inflammatory bowel disease, post-surgical pain, and experimentally induced mechanical pain (Duan et al., 2016a, 2018; Gonzalez-Lopez et al., 2018; Coates et al., 2019). Pharmacologic block of $Na_V1.8$ with small molecules inhibited native $Na_V1.8$ current [termed tetrodotoxin-resistant (TTX-R) current] and action potential firing in DRG neurons as well as pain behavioral endpoints in preclinical rodent model systems (Jarvis et al., 2007; Kort et al., 2008; McGaraughty et al., 2008; Scanio et al., 2010; Zhang et al., 2010; Payne et al., 2015; Qin et al., 2023). VX-150, a $Na_V1.8$-selective small molecule inhibitor, was the first Na_V-selective inhibitor to impart significant analgesia in the clinic in phase 2 studies of acute post-operative pain, osteoarthritis pain, and small fiber neuropathy neuropathic pain [NCT03206749 (https://clinicaltrials.gov/study/NCT03206749?tab=results); NCT03304522 (https://clinicaltrials.gov/study/NCT03304522?tab=results); https://investors.vrtx.com/news-releases/news-release-details/vertex-reports-full-year-and-fourth-quarter-2016-financial; Hijma et al., 2021]. A second $Na_V1.8$-selective small molecule, VX-548, inhibited post-operative pain in phase 2 bunionectomy and abdominoplasty studies (Jones et al., 2023). Thus, pharmacologic inhibition of $Na_V1.8$ is clinically validated as a novel analgesic mechanism of action targeting the PNS for both acute and chronic pain disorders.

Here we report on LTGO-33, a new small molecule $Na_V1.8$ inhibitor. The compound is potent with greater than 600-fold selectivity over $Na_V1.1$–$Na_V1.7$ and $Na_V1.9$. LTGO-33 exhibits state-independent inhibition with similar potencies on channels in the closed and inactivated conformations. LTGO-33 inhibits native TTX-R $Na_V1.8$ currents in non-human primate and human DRG neurons, where it reduces action potential firing. The compound inhibits $Na_V1.8$ via interaction with a novel site on the voltage-sensing domain (VSD) II extracellular region to stabilize the deactivated state. In summary, LTGO-33 represents a new $Na_V1.8$ inhibitor with a distinct mechanism of action and binding site previously undescribed in the $Na_V1.8$ pharmacologic space.

Materials and Methods

Compounds

LTGO-33 and LTGO-34 ((R-)- and (S-)-(2-(4-fluoro-2-methyl-phenoxy)-N-[3-(methylsulfonimidoyl)phenyl]-5-(trifluoromethyl)-pyridine-3-carboxamide, respectively) were synthesized at WuXi AppTec (Hong Kong) as described for example 115 as a racemic mixture (Huang et al., 2020) and enantiomers resolved by chiral supercritical fluid chromatography. Compounds were dissolved in DMSO to make concentrated stocks at 100 mM. The purity of LTGO-33 (99.7%) and LTGO-34 (97.9%) were determined by liquid chromatography-mass spectrometry.

Chemicals

All chemicals were purchased from Sigma-Aldrich (St. Louis, MO) or Thermo Fisher Scientific. Tetrodotoxin citrate (TTX) was purchased from Alomone Laboratories (Jerusalem, Israel).

Molecular Biology and Channel Constructs

cDNA clones for human ($hNa_V1.8$; NM_006514.3) and rat ($rNa_V1.8$; NM_017247.2) $Na_V1.8$ were cloned into a pcDNA3.1-P2A-mCherry mammalian expression vector (Thermo Fisher Scientific). The P2A element is a self-cleaving sequence that separates the C-terminal mCherry red fluorescent reporter from $Na_V1.8$ during translation. All mutagenesis was performed at Genscript (Piscataway, NJ), and sequences were verified by Sanger sequencing at Genscript and Laragen, Inc (Culver City, CA). The numbering of human amino acids is based on RefSeq NP_006505.4. Plasmids were transfected into ND7/23 cells using Lipofectamine 3000 (Thermo Fisher Scientific) according to the manufacturer's protocol, and cells were used for patch-clamp recordings 24 to 48 hours post-transfection.

Sequence Alignment and Structural Analysis

DNA and protein sequences were aligned using Clustal Omega (EMBL-EIB, Cambridgeshire, UK). Molecular graphics and structural analyses were performed with UCSF ChimeraX (version 1.3). A published structure of the apo $hNa_V1.8$ (PDB: 7WFW) was used to generate structural models.

DRG Preparation

Rat and Mouse DRG. Female rat and mouse DRG were purchased from BrainBits LLC (Springfield, IL) and dissociated the day after tissue collection. Mouse or rat DRG were sequentially digested in 0.12% papain for 45 minutes (BrainBits) and 0.3% collagenase Type II (Worthington Biochemical, Lakewood, NJ) for 15 minutes at 37°C in Hibernate A medium without Ca^{2+} or Mg^{2+} (BrainBits), followed by trituration with 0.05% DNAase I (Worthington) in Hibernate A medium. Cells were pelleted by centrifugation at 180 *g* for 5 minutes and washed twice with NbActiv4 (BrainBits). Dissociated neurons were plated on glass coverslips (Neuvitro, Camas, WA) coated with rat tail collagen (Cell Applications Inc, San Diego, CA) in NbActiv4 with 25 ng/mL rat nerve growth factor (Thermo Fisher Scientific). Neurons were kept at 37°C in 5% CO_2 and used for patch-clamp recordings the next day.

Dog DRG. Dog DRGs were obtained by Neuroservice USA (San Diego, CA) from all spinal levels of a male beagle dog. Procedures were carried out in accordance with the Guide for the Care and Use of Laboratory Animals as adopted and promulgated by the U.S. National Institutes of Health and approved by an Institutional Animal Care and Use Committee. DRGs were enzymatically and mechanically dissociated by methods adapted from reports (Gerhauser et al., 2012; Tongtako et al., 2017; Schwarz et al., 2020). Briefly, ganglia were dissected into small pieces and enzymatically dissociated by incubation with 0.2% hyaluronidase (Worthington), 0.2% collagenase Type 4 (Worthington), and 0.2% collagenase Type XI (Sigma) for 30 minutes at 37°C in Hibernate A without Ca^{2+} or Mg^{2+}. After 30 minutes, type I trypsin (Worthington) was added to 0.2% followed by 30-minute incubation at 37°C. The tissue was mechanically dissociated by trituration with flame-polished Pasteur pipettes after adding 0.2% DNAse I. Cells were pelleted by centrifugation at 300 *g* for 5 minutes then resuspended in NbActiv4 and plated onto glass coverslips coated with poly-D-lysine (100 μg/ml; Sigma-Aldrich) in NbActiv4 with 1% penicillin-streptomycin (Gibco) and recombinant human nerve growth factor (25 ng/mL; Axol, Coral Gables, FL) and maintained

at 37°C in 5% CO_2. Neurons were used for patch clamp recordings up to 3 days post-dissociation. All work was performed at Neuroservice USA.

Cyno DRG. Cyno DRGs were obtained by Neuroservice USA from all spinal levels of a female cynomolgus monkey. Procedures were carried out in accordance with the Guide for the Care and Use of Laboratory Animals as adopted and promulgated by the U.S. National Institutes of Health and approved by an Institutional Animal Care and Use Committee. DRGs were dissociated and plated using the same protocol as dog DRGs. Neurons were used for patch clamp recordings up to 3 days post-dissociation. All work was performed at Neuroservice USA.

Human DRG. All human tissues used for the study were obtained by legal consent from anonymous organ donors in the United States by Anabios Corporation (San Diego, CA). Anabios Corporation's procurement network includes only US-based organ procurement organizations and hospitals. Policies for donor screening and consent are established by the United Network for Organ Sharing. Organizations supplying human tissues to Anabios follow the standards and procedures established by the US Centers for Disease Control and are inspected biannually by the California Health and Human Services Agency. Donors were healthy adults without a history of pain-related disorders. Three male and two female donors were used for the voltage-clamp study, and one male and two female donors were used for the current-clamp study. Demographic details for each donor can be found in Supplemental Table 1. The DRGs were enzymatically digested using proprietary procedures that were adapted from published methods (Davidson et al., 2014; Valtcheva et al., 2016) and the isolated neurons cultured in Dulbecco's modified Eagle's medium (DMEM) F-12 supplemented with Glutamine 2 mM (Gemini Bio-Products, West Sacramento, CA), 10% FBS (Invitrogen), hNGF (10 ng/ml; Cell Signaling Technologies, Danvers, MA), GDNF (10 ng/ml; ProSpec, East Brunswick, NJ) and 1% penicillin-streptomycin (Thermo Fisher Scientific) and maintained at 37°C in 5% CO_2. Recordings were made from neurons after 2 to 4 days in culture. All neuron preparations were performed at Anabios Corporation.

Mammalian Cell Culture and Preparation

HEK293 cells stably expressing $hNa_V1.8$ (AF117907/NM_001293306)/β1 (NM_001037) (CYL3025; Eurofins DiscoverX) were grown in DMEM/F-12 + Glutamax (Thermo Fisher Scientific), 10% FBS (Sigma), 1% nonessential amino acids (NEAA; Sigma-Aldrich), and 1% penicillin-streptomycin (Thermo Fisher Scientific) with 0.625 μg/ml puromycin (Thermo Fisher Scientific), 400 μg/ml geneticin (Thermo Fisher Scientific), and 100 μg/ml hygromycin (Thermo Fisher Scientific) included as selection antibiotics. ND7/23 cells stably expressing rat $Na_V1.8$ (U53833/NM_017247) (CYL3050; Eurofins DiscoverX) were maintained in media containing DMEM + Glutamax, 1% Glutamax, 10% FBS, 1% NEAA, 1% penicillin-streptomycin, and 400 μg/mL geneticin as selection agent. The HEK293 $hNa_V1.8/\beta1$ and ND7/23 $rNa_V1.8$ stable cell lines were screened by the vendor using the ELISA-based Mycoplasma Detection kit (Roche, Penzberg, Germany) and by a PCR VenorGeM kit (Minerva Biolabs, Berlin, Germany) to confirm the absence of Mycoplasma species. Cells were not routinely monitored for mycoplasma contamination during the course of these experiments. ND7/23 cells (92090903, Sigma-Aldrich) used for transfection were maintained in media containing DMEM + Glutamax, 1% Glutamax, 10% FBS, 1% NEAA, and 1% penicillin-streptomycin. The mycoplasma status of wild-type (WT) ND7/23 cells was unknown at acquisition and cells were not routinely monitored for mycoplasma contamination. All cells were cultured at 37°C with 5% CO_2. Cells were lifted with TrypLE dissociation reagent (Thermo Fisher Scientific) and plated onto uncoated German glass coverslips (Neuvitro) with antibiotic-free media. Cells were thereafter kept at 30°C with 5% CO_2 and used 1 to 2 days after plating.

Electrophysiological Recordings

HEK293, ND7/23, Rat DRG, and Mouse DRG Voltage Clamp. HEK293 cells, ND7/23 cells, and mouse and rat DRG neurons were tested in the whole-cell configuration on manual patch clamp rigs using an Axopatch 200B amplifier (Axon Instruments, San Jose, CA) and a Digidata 1322A or Digidata 1440A digitizer (Axon) using pClamp 9.2 or 10.7 (Molecular Devices, San Jose, CA), respectively. When testing transfected cells, red fluorescence from the cleaved mCherry reporter was used to identify cells expressing $Na_V1.8$. Mouse and rat DRG neurons were selected for recording based on smoothness of the membrane. All electrophysiology data were analyzed with Clampfit 11.1 (Molecular Devices). All recordings were done at room temperature (21 – 23°C). A low-volume RC-26GLP recording chamber (Warner Instruments, Hamden, CT) was used with a gravity perfusion system flowing at a rate of 8 mL/min. The external bath solution was made of 130 mM NaCl, 15 mM TEA Cl, 1 mM $MgCl_2$, 2 mM $CaCl_2$, 10 mM HEPES, 10 mM D-glucose, and 500 nM TTX, adjusted to pH 7.4 with NaOH. LTGO-33 was added with a constant 0.1% DMSO and vehicle solutions contained 0.1% DMSO without LTGO-33. The pipette solution contained 65 mM CsF, 65 mM CsCl, 10 mM HEPES, 5 mM EGTA, 1 mM $MgCl_2$, adjusted to pH 7.4 with CsOH. Mannitol was used to adjust osmolarity, with the pipette solution kept 10 to 15 mOsm hypoosmotic relative to the bath solution. Pipettes were pulled from borosilicate glass (Sutter Instruments, Novato, CA) with a P-97 Flaming/Brown Puller (Sutter) and polished on a MF-9 Microforge (Narishige, Tokyo, Japan). When filled with intracellular solution, pipette resistances were 1.5 to 4 MΩ. Series resistance was compensated to 70% to 85% for protocols involving voltage-steps and was otherwise $<$ 10 MΩ when uncompensated. Signals were filtered at 10 kHz and digitized at 50 kHz. All measures of LTGO-33 potency used a voltage protocol with a 50 ms pulse to 0 mV from a holding potential of −80 mV at 0.5 Hz. Voltage protocols that differ are indicated in the figures.

Dog and Cyno DRG Voltage Clamp. Recordings were made using a Multiclamp 700B amplifier (Axon) and signals digitized using a Digidata 1550B (Axon), with pClamp 11.2 software (Molecular Devices) used for data acquisition and analysis. Neurons for recordings were selected based on smoothness of the membrane. The external bath solution contained 50 mM NaCl, 90 mM choline chloride, 2.5 mM KCl, 2 mM $CaCl_2$, 1.3 mM $MgCl_2$, 10 mM glucose, 10 mM HEPES, and 500 nM TTX buffered to pH 7.3. The pipette solution contained 70 mM CsF, 70 mM CsCl, 3 mM $MgCl_2$, 5 mM EGTA, 0.5 mM $CaCl_2$, 4 mM ATP, 0.3 mM GTP, and 10 mM HEPES buffered to pH 7.3. Measures of LTGO-33 potency on dog and cyno neurons were measured by a 30 ms pulse to −20 mV from a holding potential of −100 mV at 0.067 Hz. All work was performed at Neuroservice USA.

Human DRG Voltage Clamp. Voltage-clamp studies using neurons from donors #1 and #2 (Supplemental Table 1) were tested at Anabios as follows. Whole-cell patch-clamp recordings were conducted under voltage-clamp mode at room temperature (~23°C) using a HEKA EPC-10 amplifier (HEKA Elektronik, Stuttgart, Germany). Neurons for recordings were selected based on smoothness of the membrane. Data were acquired on a Windows-based computer using the PatchMaster program (v2x90.4; HEKA) and analyzed with Fit Master (HEKA) and MS Excel (Microsoft). Pipettes (1.0–2.0 MΩ) were fabricated from 1.5 mm capillary glass using a P-100 puller (Narishige) and fire polished using an MF-830 microforge (Narishige). Signals were filtered at 3 kHz and sampled at 10 kHz. A P/4 protocol was used for leak subtraction. The external bath solution contained 20 mM NaCl, 95 mM choline Cl, 3 mM KCl, 1 mM $MgCl_2$, 2 mM $CaCl_2$, 0.1 mM $CdCl_2$, 0.1 mM $NiCl_2$, 10 mM glucose, 10 mM HEPES, 20 mM TEA, and 500 nM TTX. pH was adjusted to 7.4 with N-methyl-D-glucamine. The internal pipette solution contained 135 mM CsF, 1 mM $MgCl_2$, 2 mM Na-ATP, 1 mM EGTA, 10 mM HEPES, and 10 mM phosphocreatine Tris. pH was adjusted to 7.20 with CsOH. The pipette solution was kept 25 mOsm

hypoosmotic to the bath solution. LTGO-33 potency was measured by 50 ms pulses to 0 mV from a holding potential of −80 mV at 0.5 Hz.

Voltage-clamp studies using neurons from donors #3 to #5 (Supplemental Table 1) were tested at Latigo Biotherapeutics using an identical protocol as that for rat and mouse DRG neurons except that the external bath solution was made of 30 mM NaCl, 100 mM choline Cl, 1 mM $MgCl_2$, 2 mM $CaCl_2$, 10 mM HEPES, 10 mM D-glucose, and 500 nM TTX, adjusted to pH 7.4 with NaOH.

Human DRG Current Clamp. Current-clamp studies using neurons from donors #6 to #8 (Supplemental Table 1) were tested at Anabios as follows. Whole-cell patch-clamp recordings were conducted under current-clamp mode at room temperature (~23°C) using HEKA EPC-10 amplifier. Cells for recordings were selected based on smoothness of the membrane. Data were acquired on a Windows-based computer using the PatchMaster program (HEKA) and were analyzed with Fit master (v2x90.3; HEKA) and MS Excel (Microsoft). Pipettes (1.5–3.0 MΩ) were fabricated from 1.5 mm capillary glass using a P-97 puller (Sutter). Cells were held at resting membrane potential. Signals were filtered at 3 kHz and sampled at 10 kHz. For neurons treated with LTGO-33, action potentials were induced by a train of 120 individual current steps delivered at 1, 3, and 10 Hz using current injection at 150% of baseline rheobase (the minimum current needed for stable action potential induction). For time-matched vehicle controls, action potentials were induced by a train of 50 individual current steps delivered at 10 Hz using current injection at 150% of baseline rheobase. The external solution contained 145 mM NaCl, 3 mM KCl, 1 mM $MgCl_2$, 2 mM $CaCl_2$, 10 mM HEPES, and 10 mM dextrose adjusted to pH 7.40 with NaOH. The pipette solution contained 110 mM K^+ gluconate, 20 mM KCl, 10 mM EGTA, 8 mM NaCl, 4 mM Mg-ATP, and 10 mM HEPES adjusted to pH 7.30 with KOH. The pipette solution was kept 20 mOsm hypoosmotic to the bath solution. All work was performed at Anabios Corporation.

$Na_V1.1-Na_V1.8$ Selectivity. LTGO-33 potency on $Na_V1.1-1.8$ was measured on the SyncroPatch 384PE platform (SP384PE; Nanion, Livingston, NJ) using CHO cell lines stably expressing $Na_V1.1-1.8$ ($Na_V1.1$ (CT6178), $Na_V1.2$ (CT6010), $Na_V1.3$ (CT6157), $Na_V1.4$ (CT6005), $Na_V1.5$ (CT6007), $Na_V1.6$ (CT6158), $Na_V1.7$ (CT6003), and $Na_V1.8/\beta3$ (CT6011; Charles River Laboratories). Cells were routinely monitored for mycoplasma contamination using the MycoAlert PLUS Mycoplasma Detection Kit (Lonza, Basel, Switzerland) to confirm the absence of Mycoplasma species. All test and control solutions contained 0.3% DMSO (Sigma-Aldrich) and 0.03% Pluronic F-127 (Sigma-Aldrich). The SP384PE system was used in population patch clamp mode using 8-hole Nanion 384-well Patch Clamp chips (8xM NPC-384). The bath solution contained 137 mM NaCl, 4 mM KCl, 3.8 mM $CaCl_2$, 1 mM $MgCl_2$, 10 mM HEPES, and 10 mM glucose adjusted to pH 7.4 with NaOH. The intracellular solution contained 50 mM CsCl, 90 mM CsF, 2 mM $MgCl_2$, 5 mM EGTA, and 10 mM HEPES adjusted to pH 7.2 with CsOH. Cells were held at −90 mV and a 200 ms pre-pulse to −120 mV was applied before a test pulse to +10 mV ($Na_V1.1-Na_V1.3$ and $Na_V1.8/\beta3$) or 0 mV ($Na_V1.4-Na_V1.7$) at 10 second intervals. Data acquisition and analysis were performed using the SP384PE system operation software. All work was performed at Charles River Laboratories (Cleveland, OH).

$Na_V1.9$ Selectivity. LTGO-33 potency on $Na_V1.9$ was measured on the QPatch 16X or QPatch HTS platform (Sophion, Ballerup, Denmark) using an $hNa_V1.9$ HEK293 stable cell line and analyzed with QPatch Assay software (version 5.2). Cells were monitored for mycoplasma contamination annually with a polymerase chain reaction VenorGeM kit (Minerva Biolabs) to confirm the absence of Mycoplasma species. The bath solution contained 137 mM NaCl, 4 mM KCl, 1.8 mM $CaCl_2$, 1 mM $MgCl_2$, 10 mM HEPES, and 10 mM glucose adjusted to pH 7.4 with NaOH. DMSO was held at 0.1%. The intracellular solution contained 135 mM CsF, 10 mM NaCl, 10 mM HEPES, 5 mM EGTA, 0.5 μM GTP-γS, and adjusted to pH 7.3 with KOH. Cells were held at -140 mV and current was measured with 40 ms steps to −40 mV at 10 second intervals. All work was performed at B'SYS GmbH (Witterswil, Switzerland).

Statistics and Analyses

Electrophysiology recordings were analyzed as indicated in prior sections. GraphPad Prism 10.0 was used to analyze results, perform fits, and generate plots.

Changes in DRG neuron action potential firing in response to treatment with LTGO-33 at 3 and 10 Hz and vehicle at 10 Hz were analyzed by comparing the ratio of APs remaining after treatment to the APs at baseline for each neuron. The ratios were tested with a two-tailed paired *t*-test using GraphPad Prism 10.0 with $P < 0.05$ set as the threshold for statistical significance. The ratios were plotted, and the geometric mean of ratios reported along with 95% confidence intervals (CIs).

Action potential parameters were derived from measurement of the rheobase action potential, (i.e., that evoked by the minimum current amplitude needed to elicit an action potential) and calculated in Clampfit 11.1. The peak (maximum positive voltage) and subsequent trough (maximum negative voltage) were identified and the difference between them reported as the absolute amplitude (mV). The width of the action potential at 50% of the absolute amplitude was reported as half-width (ms). The maximum rise slope (mV ms^{-1}) and maximum decay slope (mV ms^{-1}) were calculated as the greatest rising and falling slopes, respectively. These parameters were plotted as pairs before and after treatment and compared with a two-tailed paired *t*-test using GraphPad Prism 10.0 with $P < 0.05$ set as the threshold for statistical significance. The differences (for absolute amplitude and half-width) or ratios (for rheobase and maximum rise and decay slope) were plotted and the arithmetic (for differences) or geometric (for ratios) means were reported along with 95% confidence intervals.

Concentration-response data were averaged by concentration and fit with the nonlinear regression fit: "[Inhibitor] vs response – variable slope (four parameters)" using the equation

$$Y = Bottom + \frac{Top - Bottom}{1 + \left(\frac{IC_{50}}{X}\right)^{Hill\ slope}} \quad (1)$$

where Top was set to equal 1.0 and Bottom to 0.0, and X is the concentration. 95% confidence intervals were reported for all IC_{50}s. Measurements of single point IC_{50}s additionally set the Hill slope equal to −1.

Relationships between conductance and voltage (GV), inactivation and voltage (SSI), and disinhibition and voltage were fit with the Boltzmann equation:

$$Y = Bottom + \frac{Top - Bottom}{\left(1 + \exp\left(\frac{V_{50} - X}{\frac{RT}{zF}}\right)\right.} \quad (2)$$

where T is temperature in Kelvin, z is the valence, R is the universal gas constant (8.314 J mol^{-1} K^{-1}), and F is the Faraday constant (9.648×10^4 C mol^{-1}). 95% confidence intervals were reported for all Boltzmann fits.

Single-exponential fits were performed with the nonlinear regression fit: "one phase decay" using the equation

$$Y = (Y0 - Plateau) * \exp(-K * X) + Plateau \quad (3)$$

where K is the rate constant and its reciprocal τ (tau), the time constant, was reported. 95% confidence intervals were reported for all single-exponential tau values.

All fits were made to the averaged data at each concentration or time point, and values derived from fitting approaches (i.e., tau, IC_{50}, $V_{1/2}$) are reported in the text with 95% confidence intervals. Counts for *n* reported in the text reflect biologic replicates. In cases where *n* was variable between concentrations, the range of *n* is indicated in the text and specific counts can be found in Supplemental Tables 2–6.

Otherwise, the provided n value indicates all concentrations had the given n. All plotted points represent arithmetic mean and error bars represent S.D., unless otherwise noted.

This study was not designed to test a prespecified statistical null hypothesis and a prewritten statistical protocol was not used. As a result, this work should be considered exploratory.

Results

LTGO-33 Is a Potent and Selective $Na_V1.8$ Inhibitor

To assess LTGO-33 (structure shown in Fig. 1A) potency against human $Na_V1.8$ ($hNa_V1.8$) in heterologous cells, we used manual patch clamp electrophysiology with a conventional two-pulse voltage-clamp protocol in HEK293 cells stably co-expressing $hNa_V1.8$ and the $\beta1$ accessory subunit (Fig. 1B, inset). The first test pulse measured inhibition from the closed or resting state, while the second pulse measured inhibition from an inactivated state, following an 8-second hold at −45 mV, which approximates the $V_{1/2}$ of inactivation (Supplemental Fig 1A, Supplemental Table 7).

LTGO-33 exhibited an IC_{50} of 33 nM (95% CI: 24 to 44 nM, $n = 10$ cells) from the closed state and 24 nM (95% CI: 19 to 30 nM, $n = 10$ cells) from an inactivated state (Fig. 1B and C). LTGO-33 showed no overt state dependence, in that potencies were comparable between both resting and inactivated states. LTGO-33 did not affect the voltage-dependence of activation (Supplemental Fig. 1B). The rate of channel inactivation remained unaffected by LTGO-33, indicating that inhibition was not due to acceleration of inactivation and further supporting the state-independent mode of inhibition (Supplemental Fig. 1C). Given this, we performed all further measures of potency using voltage protocols that interrogate the closed state to shorten recording time and minimize current rundown.

We next evaluated LTGO-33 selectivity against the human Na_V family. LTGO-33 was tested against $hNa_V1.1$–$hNa_V1.9$ using automated patch-clamp platforms (Fig. 1D). The potency of LTGO-33 against $hNa_V1.8$ was 44 nM (95% CI: 38 to 52 nM, $n = 6-8$ wells per concentration, Supplemental Table 2) while the potencies against $hNa_V1.1$–$hNa_V1.7$ and $hNa_V1.9$ were over 30 μM ($n = 2-7$ wells per concentration, Supplemental Table 2), corresponding to a minimum selectivity over 600-fold. The fold-selectivity is likely considerably higher, as LTGO-33 inhibited all non-$hNa_V1.8$ isoforms by less than 25% at 30 μM. The enantiomer, LTGO-34, showed similar potency against $hNa_V1.8$ in HEK293 cells as LTGO-33 (IC_{50} of 34 nM, 95% CI: 31 to 38 nM, $n = 7$ cells), a high degree of selectivity among the human Na_V family (selectivity over 450-fold), and a state-independent inhibition profile (IC_{50} of 24 nM from an inactivated state, 95% CI: 21 to 26 nM, $n = 7$ cells), indicating chirality of the sulfoximine moiety had no impact on these pharmacologic parameters (Supplemental Fig. 2A–D).

LTGO-33 was also tested against immortalized rat DRG/mouse hybridoma neuronal ND7/23 cells stably expressing the rat isoform of $Na_V1.8$ ($rNa_V1.8$). Compared with $hNa_V1.8$ expressed in HEK293 cells (IC_{50} of 14 nM, 95% CI: 12 to 16, $n = 6$ cells), the potency of LTGO-33 was markedly right-shifted, with an IC_{50} of 5.7 μM (95% CI: 4.1 to 8.7 μM, $n = 4$ cells), representing a 400-fold drop in potency compared with $hNa_V1.8$ (Fig. 1E). To extend this finding, we tested the potency of LTGO-33 against native $Na_V1.8$ channels that generate TTX-R currents in DRG neurons from several rodent and nonrodent species. LTGO-33 inhibited TTX-R currents in primary DRG neurons from human (male donors: IC_{50} of 110 nM, 95% CI: 92 to 120 nM, $n = 3-15$ neurons per concentration; female donors: IC_{50} of 120 nM, 95% CI: 100 to 140 nM, $4-6$ neurons per concentration, Supplemental Table 3) and cynomolgus monkey (IC_{50} of 100 nM, 95% CI: 71 to 150 nM, $n = 6$ cells) but was markedly less effective on DRG neurons from dog (IC_{50} >10 μM, $n = 6$ cells), rat (IC_{50} >30 μM, $n = 7$ cells), and mouse (IC_{50} >30 μM, $n = 8$ cells) (Fig. 1F). We observed no sex-dependent difference in LTGO-33 potency on human DRG neurons. Potency in human and cynomolgus monkey neurons was comparable, and potency in human neurons decreased around threefold compared with HEK293 cells.

LTGO-33 Decreased Excitability of Human DRG Neurons

We next assessed the effect of LTGO-33 on action potential firing in nociceptive neurons. Cultured DRG neurons from three separate human donors (one male, two female) were prepared, and the rheobase, or the minimum current injection required to elicit an action potential, was determined. Neurons were stimulated with 20 ms current injections at 150% rheobase with various stimulation frequencies before and after application of 200 nM LTGO-33, a concentration twofold higher than the male or female human DRG neuron IC_{50} (Fig. 2A, inset). Importantly, TTX was not included in these experiments to provide a more physiologically relevant context where both TTX-R and tetrodotoxin-sensitive (TTX-S) conductances can contribute to the action potential upstroke (Blair and Bean, 2002).

Human DRG neurons with resting membrane potentials around −65 mV (Supplemental Fig 3A) showed a frequency-dependent inhibition of excitability following LTGO-33 treatment, with a statistically significant reduction of action potentials at 10 Hz (3 Hz: treatment/baseline ratio: 0.81, 95% CI: 0.57 to 1.1, $P = 0.19$, $n = 10$ neurons; 10 Hz: treatment/baseline ratio: 0.53, 95% CI: 0.29 to 0.94, $P = 0.034$, $n = 10$ neurons) while time-matched vehicle controls showed no decrease in action potentials at 10 Hz (treatment/baseline ratio: 1.0, 95% CI: 0.83 to 1.2, $P = 0.95$, $n = 4$ neurons) (Fig. 2A and B). Furthermore, LTGO-33 treatment increased the rheobase of hDRG neurons (treatment/baseline ratio: 1.17, 95% CI: 1.07 to 1.28, $P = 0.0040$) (Fig. 2C). Vehicle-treated neurons showed little change in AP firing while LTGO-33-treated neurons showed a broad range of responses with some unaffected and others markedly inhibited (Fig. 2D and E, Supplemental Fig. 3B and C). Analysis of AP parameters including amplitude, half-width, and the maximum rise and decay slopes revealed a significant change in the maximum rise slope (treatment/baseline ratio: 0.78, 95% CI: 0.66 to 0.93, $P = 0.0121$) (Fig. 2F–I, Supplemental Table 8) for LTGO-33-treated neurons. Phase plots of LTGO-33-treated neurons showed a slowed AP upstroke that was not observed in vehicle-treated neurons (Fig. 2J and K).

The Predicted Binding Pocket for LTGO-33 Is Contained within VSDII

Given the state-independent mode of LTGO-33 inhibition, we next conducted experiments to elucidate the compound binding site. To this end, we exploited the species selectivity of LTGO-33. Human and rat $Na_V1.8$ protein sequences are

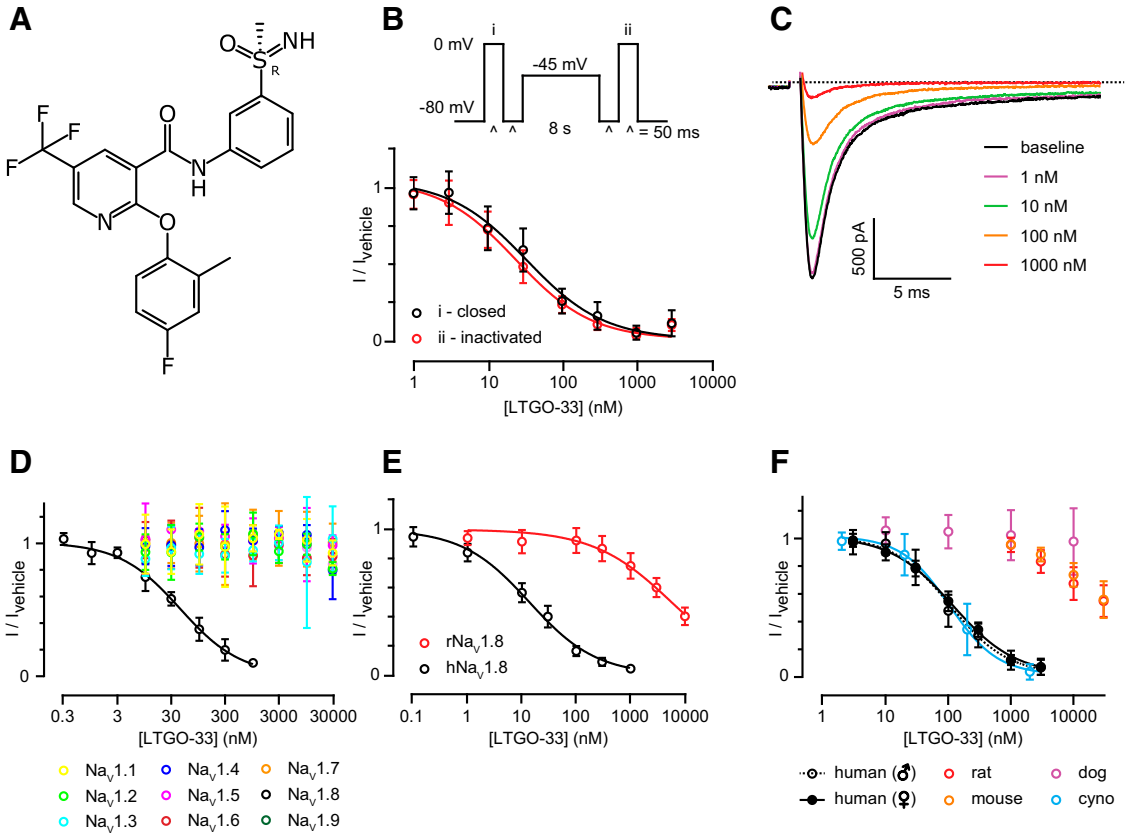

Fig. 1. LTGO-33 potently and selectively inhibits human $Na_V1.8$. (A) Structure of LTGO-33. (B) Voltage protocol (top) used to generate concentration-response curves for LTGO-33 (bottom) on $hNa_V1.8$ stable cell line. Black shows inhibition of closed or resting channels and red shows inhibition following entry of channels into inactivated states. Mean ± S.D. $n = 5$ cells per concentration. (C) Example traces of $hNa_V1.8$ inhibition by escalating concentrations of LTGO-33. Currents elicited by a 50 ms pulse to 0 mV from a holding potential of −80 mV. (D) LTGO-33 potency against other human Na_V isoforms. Mean ± S.D. $n = 2-8$ wells per concentration (Supplemental Table 2). (E) Potency of LTGO-33 on $hNa_V1.8$ HEK (black) and $rNa_V1.8$ ND7/23 (red) stable cell lines. Mean ± SD. $n = 6$ cells per concentration for $hNa_V1.8$ HEK and $n = 4$ for $rNa_V1.8$ ND7/23. (F) Potency of LTGO-33 on the TTX-R component of DRG neurons from human (male and female), cyno monkey, dog, rat, and mouse. Mean ± S.D. $n = 6$ neurons for dog and cyno, $n = 7$ neurons for rat, $n = 8$ neurons for mouse, and $n = 3-15$ neurons per concentration for human (Supplemental Table 3).

83.1% identical (Supplemental Fig. 4A), yet LTGO-33 was 400-fold less potent against the rat isoform. By using $rNa_V1.8$ as an insensitive host background, we replaced regions with $hNa_V1.8$ to recover LTGO-33 activity. We separately transplanted the voltage-sensing domain (comprising the transmembrane regions S1–S4), for domain I (VSDI), domain II (VSDII), domain III (VSDIII), and domain IV (VSDIV) (Fig. 3A). When transiently expressed in ND7/23 cells, $rNa_V1.8$ containing human VSDI, VSDIII, and VSDIV were indistinguishable from the WT $rNa_V1.8$ in terms of LTGO-33 potency [VSDI, VSDIII, VSDIV all $IC_{50} > 30$ μM ($n = 6$ cells), WT $rNa_V1.8$ $IC_{50} > 30$ μM ($n = 5$ cells)] while $rNa_V1.8$ containing human VSDII showed a marked gain of function with an IC_{50} of 84 nM (95% CI: 72 to 97 nM, $n = 6$ cells) (Fig. 3B and C). Similarly, a chimera containing the full voltage-sensor domain plus pore region (S1–S6) of human DII revealed an IC_{50} of 74 nM (95% CI: 58 to 95 nM, $n = 5$ cells) while full DI, DIII, and DIV chimeras all had IC_{50} values greater than 30 μM ($n = 6$ cells) (Supplemental Fig. 5A–C). No additional inhibition was observed with inclusion of the S5–S6 pore region of DII, suggesting the pore domain does not contribute to the LTGO-33 binding site. These data suggest that the LTGO-33 binding site resides within VSDII.

To further narrow down the putative binding site within VSDII, we aligned rat and human VSDII sequences (Fig. 3D) and generated a minimal gain-of-function chimera containing selected $hNa_V1.8$ VSDII residues introduced into the $rNa_V1.8$ backbone. By comparing the published structures of mammalian Na_V channels ($Na_V1.5$: PDB 6UZ3; $Na_V1.7$: PDB 6N4I; $Na_V1.8$: PDB 7WFW), we excluded amino acids whose side chains were oriented into the membrane, instead focusing on differences within the extracellular VSD cleft. The minimal chimera constructed changed six residues in the S1–S2 loop, three residues at the extracellular terminus of S3, and a single residue near the top of S4 adjacent to the first gating charge, R1 (Fig. 3D, orange-shaded residues). LTGO-33 inhibited this minimal chimera with an IC_{50} of 150 nM (95% CI: 130 to 180 nM, $n = 6$ cells), roughly half the potency of the full VSDII chimera (84 nM) (Fig. 3E and F). Taken together, these results strongly support a putative binding site for LTGO-33 in the extracellular cleft of VSDII.

Alignment of the protein sequences of rat and dog $Na_V1.8$, which are both less sensitive to LTGO-33 inhibition, with $hNa_V1.8$ revealed sequences unique to $hNa_V1.8$ that may play a prominent role in compound inhibition. Two amino acids in the S1–S2 loop (Pro691 and Thr692), Val746 at the top of S3 and Ser757 at the top of S4, are only present in

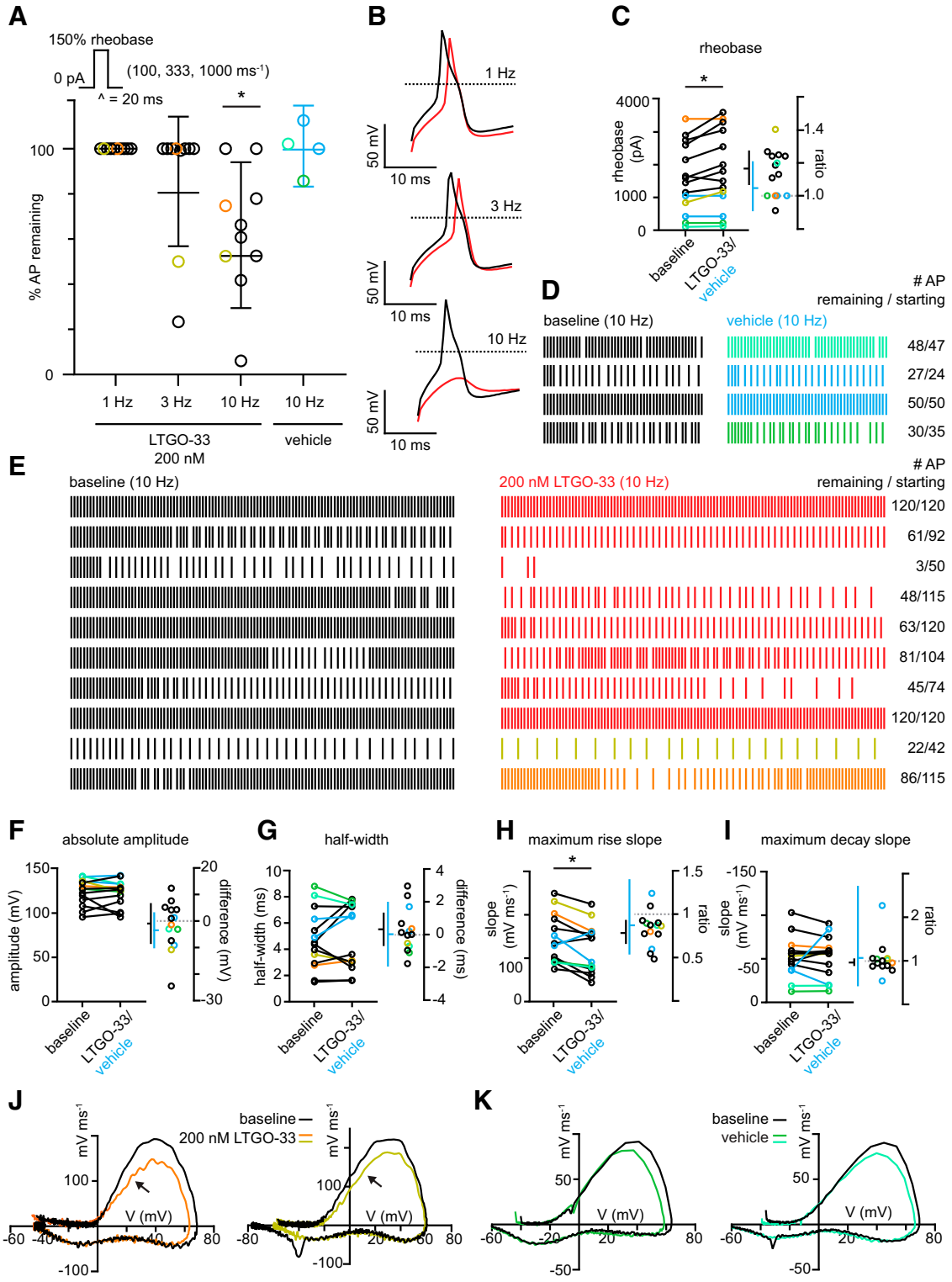

Fig. 2. LTGO-33 inhibits human DRG neuron action potential firing. (A) Current clamp protocol (top) where hDRG neurons were stimulated with 20 ms current injections to 150% rheobase at 1, 3, and 10 Hz frequencies for a total of 120 pulses (or 50 pulses for time-matched vehicle controls). Bottom, the percentage of action potentials remaining relative to baseline following application of 200 nM LTGO-33 (black) or time-matched vehicle control (blue). Orange and mustard circles specify two LTGO-33-treated neurons shown in J while green and teal specify two vehicle-treated neurons shown in K. Geometric mean ± 95% confidence intervals. Asterisk indicates $P < 0.05$. In all panels, $n = 10$ for LTGO-33-treated neurons and $n = 4$ for time-matched vehicle controls. (B) Example traces of action potentials before (black) and after (red) 200 nM LTGO-33 at 1, 3, and 10 Hz. Traces taken from the first sweep of a single neuron. Dotted lines indicate 0 mV. (C) Rheobase of hDRG neurons at baseline (black) and after treatment (color). Left shows paired comparisons and right shows ratios (treatment/baseline). Horizontal line shows geometric mean and vertical line shows the 95% confidence intervals. Asterisk indicates $P < 0.05$. (D) Raster plot showing action potentials in response to 50 stimulations delivered at 10 Hz for vehicle-treated neurons. Baseline firing is shown on left in black; vehicle control is shown on right in cool colors. Right margin indicates number of action potentials remaining/starting. (E) Raster plot showing action potentials in response to 120 stimulations delivered at 10 Hz for LTGO-33-treated neurons. Baseline firing is shown on left in black, after LTGO-33 treatment on right in warm colors. Right margin

$hNa_V1.8$ (Supplemental Fig 5D). To evaluate if these residues impacted LTGO-33 inhibition, we generated reversion mutations in which these positions were mutated back to the rat sequence from the minimal rat−human VSDII chimera. Mutation of P691D and T692A did not lose activity, while V746A resulted in 6-fold decreased activity and S757T resulted in 2.5-fold decreased activity (Table 1, Supplemental Fig 5E). These data suggest a critical role of the S3−S4 region for LTGO-33 inhibition of $hNa_V1.8$.

Amino Acids in S1, S3, and S4 VSDII Contribute to LTGO-33 Inhibition

To identify specific amino acids in VSDII required for LTGO-33 inhibition, we performed site-directed mutagenesis using an alanine scan approach through regions predicted to line the VSDII extracellular cleft based on a published structure of $hNa_V1.8$ (Fig. 4A and B) (Huang et al., 2022). We focused more on the S3−S4 region than the S1−S2 region given the minimal effect of the S1−S2 reversion mutations described earlier and the sequence differences between $hNa_V1.8$ and other hNa_V proteins in the S3−S4 region that may explain the high degree of isoform selectivity observed (Supplemental Fig 4C). Each of the S4 gating charges (Arg/Lys) were also independently mutated to alanine and glutamine.

Single point mutations of $hNa_V1.8$ were transiently expressed in ND7/23 cells and currents measured following treatment with 100 nM LTGO-33, corresponding to a concentration that inhibited about 75% of WT $hNa_V1.8$ (Supplemental Table 9). Extrapolated IC_{50} values were plotted along with the individual cell responses to LTGO-33 (Fig. 4C). The point mutants with the largest IC_{50} shifts were observed in the extracellular S3−S4 linker, one residue in S1 (M682A) and the R1 gating charge (R756Q) in S4, whereas point mutants in gating charges R2, R3, K4, and K5 were nominally impacted. The mutations showing the largest effects following 100 nM LTGO-33 application, defined as fivefold or greater reductions in IC_{50}, including the R756Q first gating charge and selected surrounding residues were chosen for full IC_{50} determinations (Fig. 4D, Supplemental Fig. 6A, Table 2, Supplemental Table 10) and comparison of the single point and full IC_{50}s showed agreement ($r^2 = 0.46$) (Supplemental Fig 6B). Mapping these residues onto the reported cryo-EM structure of $hNa_V1.8$ (Huang et al., 2022) illustrated a potential LTGO-33 binding pocket comprising the extracellular cleft of VSDII formed by S1, S3, S4 helices and S3−S4 linker region (Fig. 4E).

LTGO-33 Stabilizes the Deactivated State of VSDII

Having shown that LTGO-33 interacts with the VSDII S3−S4 region and inhibition was state-independent, we sought to further understand the mechanism of action of channel inhibition. As peptide toxins from animal venoms have also been reported to interact with the VSDII S3−S4 linker region of Na_V channels with higher potency for the deactivated state (Bosmans et al., 2008; Xu et al., 2019), we hypothesized that LTGO-33 binds to and stabilizes the deactivated (or down state) of VSDII.

Since strong depolarizations can reverse peptide toxin inhibition of Na_V channels (Edgerton et al., 2008; Sokolov et al., 2008; Moyer et al., 2018) indicating removal or release of the peptide from the binding pocket, we sought to determine if LTGO-33 bound to the deactivated state could be removed from $hNa_V1.8$ using strong depolarizing voltages in HEK293 cells stably expressing $hNa_V1.8$. Using 500 ms steps from −60 to +60 mV followed by a test pulse to 0 mV, we observed progressive recovery of $hNa_V1.8$ current in the presence of 100 nM LTGO-33 at depolarized potentials (Fig. 5A). These results were plotted against a conductance-voltage or G-V curve of the channel in the absence of compound (Supplemental Fig. 1A) and fit with the Boltzmann equation. The voltage-dependence of disinhibition had a $V_{1/2}$ of −3.6 mV (95% CI: −7.0 to −0.3 mV, $n = 8$ cells), 12 mV hyperpolarized relative to the +8.9 mV $V_{1/2}$ (95% CI: 7.5 to 10 mV) of the G-V curve. The voltage-dependence of disinhibition, with a clear plateau, suggests this effect is driven by the movement of the DII voltage sensor. The left shifted $V_{1/2}$ of disinhibition may reflect the movement of DII itself, which voltage-clamp fluorometry measurements have shown to be hyperpolarized relative to the G-V curve in other sodium channels (Silva and Goldstein, 2013; Varga et al., 2015). A conceptual model presented in Fig. 5B illustrates the proposed mechanism of inhibition whereby LTGO-33, depicted as L, interacts with and stabilizes the deactivated state of VSDII, depicted as D, as opposed to the activated state, depicted as A.

We examined the preference of LTGO-33 for the deactivated (down) state versus the activated (up) state of VSDII. To do so, we applied 100 nM LTGO-33 for 15 seconds while holding channels either at −100 mV or +20 mV to place VSDII in the deactivated or activated state, respectively, in $hNa_V1.8$-expressing HEK293 cells (Fig. 5C and D). A prepulse to +0 mV established a baseline current magnitude and post-pulses to +0 mV assessed the fraction of channels inhibited. For the protocol holding at +20 mV, the first post-pulse measured the inhibition of channels that recovered from fast inactivation, while the second post-pulse added 1 second after the first measured inhibition of channels that recovered from slow inactivation. After the −100 mV hold, LTGO-33 application inhibited channels by 75% ± 4.6% ($n = 8$ cells) while the vehicle-treated (0.1% DMSO) showed no change ($n = 8$ cells) (Fig. 5C). After the +20 mV hold, both LTGO-33 (47% ± 4.8%, $n = 7$ cells) and vehicle-treated (43% ± 2.1%, $n = 7$ cells) cells showed similar levels of inhibition following the first post-pulse (Fig. 5D), whereas vehicle-treated cells recovered to 82% ± 4.5% ($n = 7$ cells) of the starting current and LTGO-33-treated cells further decreased to 30% ± 2.4% ($n = 7$ cells) of the starting current following

indicates number of action potentials remaining/starting. (F−I) AP parameters at baseline (black) and after treatment (color). Left panels show paired comparisons and right panels show differences (treatment – baseline) for amplitude (F) and half-width (G) or ratios (treatment/baseline) for maximum rise (H) and decay slopes (I). Horizontal line shows arithmetic or geometric mean for differences and ratios, respectively, and vertical line the 95% confidence intervals. Asterisk indicates $P < 0.05$. (J) Phase plots showing the slope of the action potential waveform for two hDRG neurons at baseline (black) and after treatment with 200 nM LTGO-33 (color). Black arrows indicate the slowed rate of the AP upstroke. Orange and mustard indicate individual neurons highlighted in previous panels. (K) Phase plots showing the slope of the action potential waveform for two hDRG neurons at baseline (black) and after vehicle (color). Green and teal indicate individual neurons highlighted in previous panels.

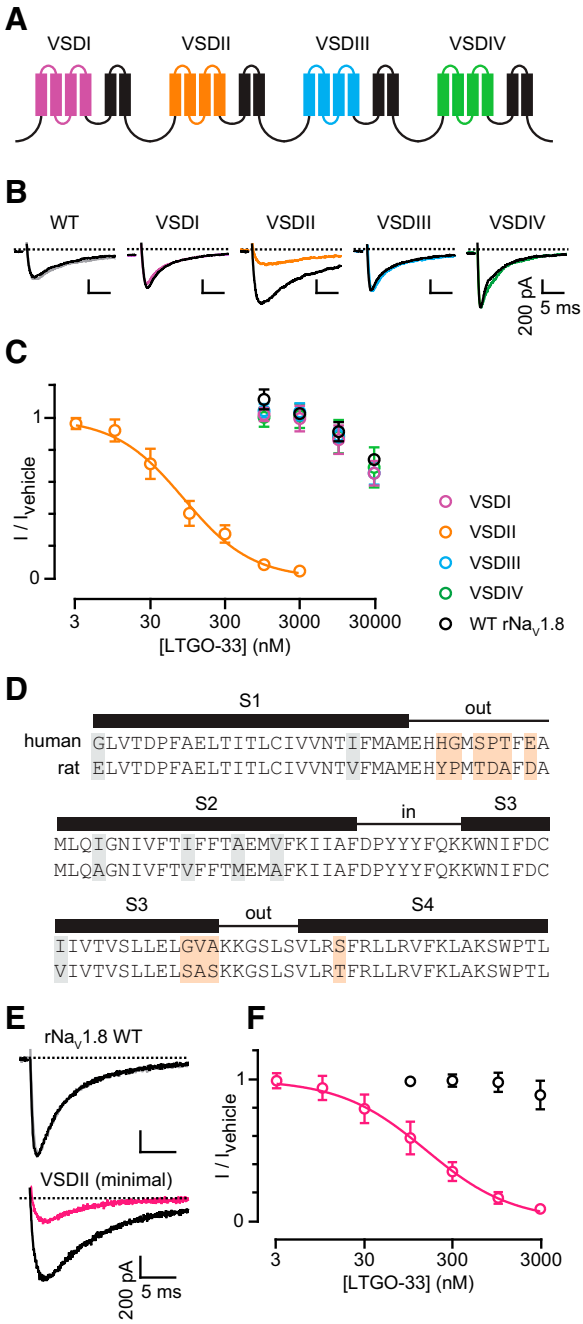

Fig. 3. Effect of LTGO-33 on human $Na_V1.8$ VSDs swapped into rat $Na_V1.8$. (A) Schematic depicting the transfer of $hNa_V1.8$ VSDI-IV (colored) into the $rNa_V1.8$ backbone (black). (B) Example traces of LTGO-33 on $Na_V1.8$ currents in WT rat and human-rat chimeric channels. Black traces show the currents before and color traces show the currents after LTGO-33 (300 nM for VSDII, 3 μM for VSDI, VSDIII, VSDIV, and WT $rNa_V1.8$). Scale bars are 5 ms on the horizontal axis and 200 pA on the vertical axis. (C) Potency of LTGO-33 on WT rNa_V 1.8 (black) and human-rat chimeras (color). Mean ± S.D. n = 6 cells for each concentration. (D) Alignment of human and rat $Na_V1.8$ VSDII. Thick black bars above denote transmembrane helices S1–S4 and thin black lines extramembrane linkers. Feature boundaries were adopted from the Uniprot entry for $Na_V1.8$ (Q9Y5Y9). Highlighted amino acids are different between human and rat $Na_V1.8$: gray residues were unchanged and orange residues were changed to create the minimal VSDII chimera. (E) Example traces of LTGO-33 inhibition on WT $rNa_V1.8$ (top, 3 μM) and the VSDII minimal chimera (bottom, 300 nM). Scale bar represents 5 ms on the horizontal axis, 200 pA along the vertical. (F) Concentration-response data for LTGO-33 on the VSDII minimal chimera and WT $rNa_V1.8$. Mean ± S.D. n = 6 cells per concentration.

TABLE 1
LTGO-33 IC_{50} values for VSDII minimal chimera and reversion mutants
Channels transiently expressed in ND7/23 cells were tested using manual patch clamp electrophysiology.

System	IC_{50} (nM)	95% CI (nM)	n (cells used for IC_{50})
WT $rNa_V1.8$	>3000		3
VSDII minimal	140	120 – 170	5
P691D T692A	140	130 – 170	4
V746A	840	680 – 1000	4
S757T	360	300 – 420	4

the second post-pulse. As both LTGO-33- and vehicle-treated cells showed similar levels of remaining current after the 15 s hold, inhibition likely arose not from compound binding to $hNa_V1.8$ but instead from channel accumulation in the slow inactivated state. Following the second post-pulse, vehicle-treated cells largely recovered from slow inactivation while LTGO-33-treated cells showed inhibition similar to levels observed with the −100 mV 15 s pulse. The results of this experiment suggest that LTGO-33 rapidly and preferentially binds the deactivated conformation of VSDII.

Next, we studied the kinetics of inhibition and disinhibition. To assess the time dependence of disinhibition we employed a protocol similar to the one used for testing interaction with the activated state, using a +40 mV hold ranging from 10 ms to 1 s in duration (Fig. 5E). Vehicle-treated cells showed no change in current magnitude following short durations and began to diminish as the +40 mV hold approached 1 s, possibly due to entry of channels into the slow inactivated state (Supplemental Fig. 7A). Cells that had been pretreated with 100 nM LTGO-33 showed a progressive recovery up to 55% (95% CI: 52 to 57%, n = 6 cells) of the starting current compared with precompound levels (Fig. 5E). To measure recovery of inhibited channels only, we subtracted the current remaining after application of 100 nM LTGO-33. A single-exponential fit to this recovery curve revealed that LTGO-33 dissociated from the activated VSDII conformation with a tau of 60 ms (95% CI: 47 to 78 ms, n = 6 cells). Complete recovery of inhibited current may be precluded by accumulation of channels in inactivated states during the increasingly long depolarization periods.

To measure the kinetics of binding to the deactivated state we held channels at +40 mV for 500 ms to remove LTGO-33, followed by a −80 mV recovery period extending from 1 ms to 1 s in duration (Fig. 5F). Currents during an initial phase of durations up to 10 milliseconds were the same between 100 nM LTGO-33-treated and vehicle-treated cells, likely corresponding to recovery from fast inactivation (Fig. 5F, Supplemental Fig. 7B). However, as the vehicle-treated cells reached a plateau, a second component emerged in the LTGO-33-treated cells as current decreased from compound reinhibiting in the deactivated state. A single-exponential fit to the latter phase (from 20 ms to 1 s) revealed a tau of 580 ms (95% CI: 290 to 2800 ms, n = 6 cells). Finally, following inhibition of $hNa_V1.8$ by 100 nM LTGO-33, we washed compound off while using brief depolarizations to monitor recovery from inhibition. Vehicle solution was rapidly (8 ml/min) flowed through the recording chamber and the observed rate of recovery had a tau of 22 seconds (95% CI: 18 to 28 seconds, n = 8 cells) (Fig. 5G). Taken together, these mechanism of action studies indicate that LTGO-33 preferentially interacts with the deactivated state over the activated state of VSDII.

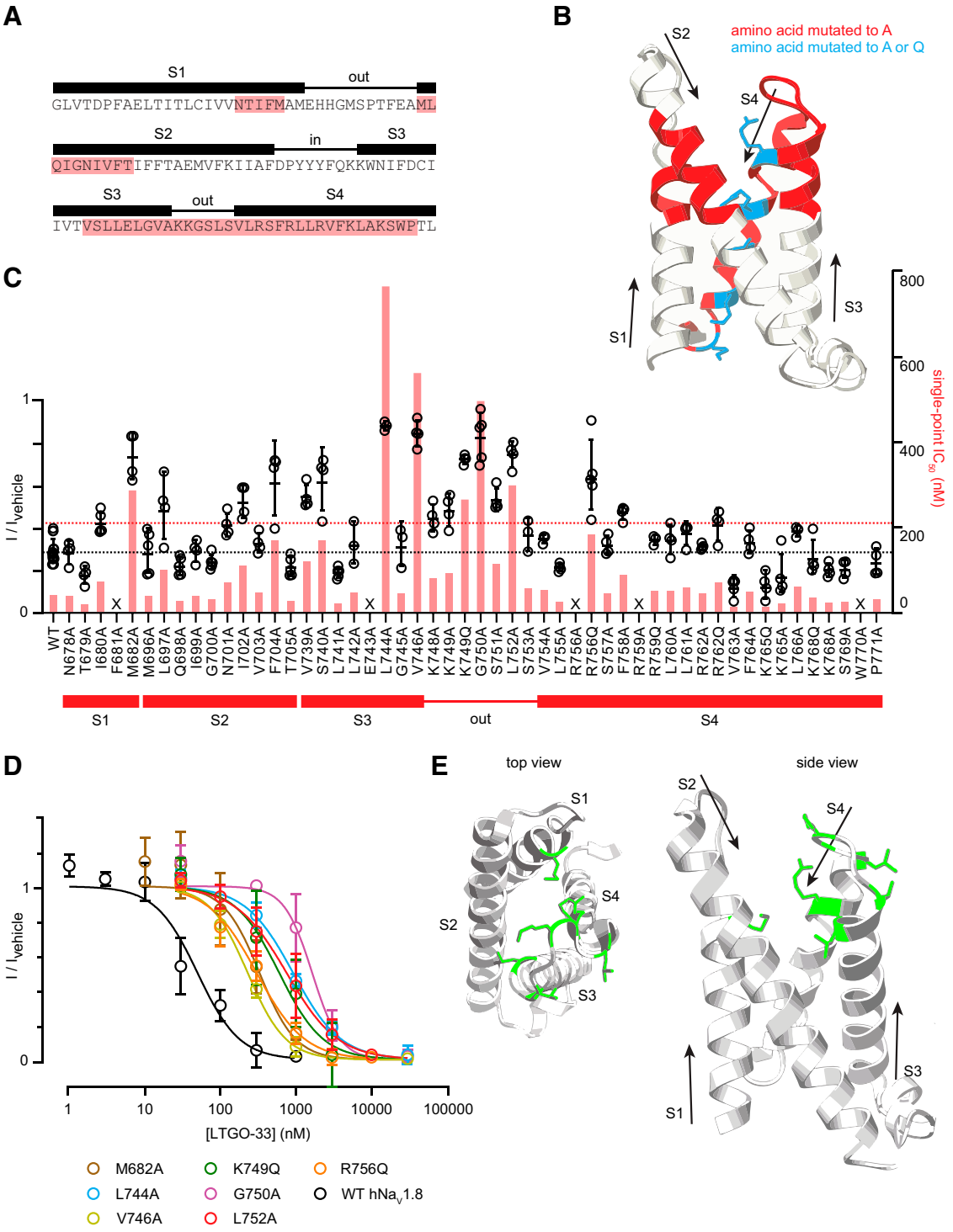

Fig. 4. Alanine scan approach maps the LTGO-33 interaction site to VSDII. (A) Sequence of hNa$_V$1.8 VSDII. Thick black bars indicate the S1, S2, S3, and S4 transmembrane segments and thin black lines extramembrane linkers. Feature boundaries were adopted from the Uniprot entry for Na$_V$1.8 (Q9Y5Y9). Highlighted residues were individually mutated to Ala or Gln. (B) Location of mutated amino acids indicated on hNa$_V$1.8 VSDII in apo-hNa$_V$1.8 cryo-EM structure (PDB 7WFW). Orientation depicts the extracellular surface at top and intracellular surface at bottom. Cyan indicates residues changed to Ala or Gln, and red indicates residues changed to Ala. (C) Potency of LTGO-33 on hNa$_V$1.8 mutants derived from single point inhibition. Black open circles indicate individual cell responses to treatment with 100 nM LTGO-33. Geometric mean ×/÷ geometric S.D. Dotted black line indicates geometric mean of WT hNa$_V$1.8 response to 100 nM LTGO-33. Red bars represent IC$_{50}$ calculated from fraction of current remaining. Dotted red line indicates fivefold threshold used to identify mutants for full IC$_{50}$ determination. $n = 3 - 5$ cells per mutant, $n = 14$ for WT hNa$_V$1.8. X denotes mutations that did not express detectable current. (D) Potency of LTGO-33 on mutations with fivefold or greater change in single-point IC$_{50}$. Mean ± S.D. $n = 2 - 6$ cells per concentration (Supplemental Table 4). (E) Locations of mutations with fivefold or greater change in single-point IC$_{50}$ (lime green) mapped onto hNa$_V$1.8 VSDII (from PDB 7WFW). Left is view from top (extracellular surface) and right from side (within membrane with extracellular surface at top and intracellular surface at bottom).

TABLE 2
LTGO-33 full IC_{50} values for $hNa_V1.8$ VSDII mutations
Channels transiently expressed in ND7/23 cells were tested using manual patch clamp electrophysiology.

Construct	IC_{50} (nM)	95% CI (nM)	*n* (cells used for IC_{50})
WT $hNa_V1.8$	50	36 – 69	6
M682A	330	250 – 450	9
L744A	920	820 – 1000	5
V746A	230	200 – 270	6
K749Q	600	400 – 900	5
G750A	1600	1300 – 2000	5
L752A	760	610 – 930	5
R756Q	300	260 – 350	6

LTGO-33 Exhibits Minimal Reverse-Use Dependence under Physiologic Conditions

Reverse-use dependence, where high frequency depolarizations can displace a compound from its binding pocket and partially reverse compound-mediated inhibition, was described for the $Na_V1.8$ inhibitors A-803467 and A-887826 (Browne et al., 2009; Jo et al., 2023). If reverse use dependence manifests during high-frequency action potential firing in pain states, compound inhibition could diminish and impact analgesia efficacy. Given that LTGO-33 can be removed from activated VSDII in the millisecond time frame, we sought to understand if this could manifest as reverse-use dependence at various frequencies. In the temporal context of a nociceptor firing action potentials spontaneously or in response to algogenic stimuli, this process would be driven by the balance between compound dissociation during brief depolarizations and reinhibition in the interval between action potentials. To understand this balance, we used a 10 Hz protocol that employed a depolarizing step to +20 mV for increasing durations (Fig. 6A, inset). The durations doubled from 5 to 80 ms, increasing the relative proportion of time channels spend in the activated versus deactivated states. For example, a 5 ms hold at +20 mV would correspond to channels residing in an activated state for 5% and deactivated state for 95% of the total duration of recording. 10 Hz was selected as a physiologically relevant frequency at which LTGO-33 inhibited hDRG neuron action potential firing.

Vehicle-treated HEK293 cells stably expressing $hNa_V1.8$ maintained near full currents after 40 pulses up to 40% of the time in the activated state and showed a slight decrease at 80% of the time in the activated state, suggesting that 20 ms may limit recovery time after 80 ms depolarizing pulses (Fig. 6A). Cells treated with 100 nM LTGO-33, however, showed current recoveries of the inhibited current that increased with the fraction of time channels spent at +20 mV (Fig. 6B). Plotting the fraction of current recovered as a function of time spent at depolarized potentials highlighted recovery from inhibition with more time spent in the activated state in the continued presence of LTGO-33 (Fig. 6C).

To quantitate reverse-use dependence using more physiologically relevant recording conditions, we performed voltage-clamp experiments using an action potential waveform at various frequencies from 1 to 40 Hz in ND7/23 cells transiently expressing $hNa_V1.8$ and challenged with 100 nM LTGO-33 (Fig. 6D, top). Currents resolved as two peaks attributable to an initial peak of sodium influx (labeled i) that decreased as the voltage neared the sodium equilibrium potential and a second peak of sodium influx (labeled ii) that increased as cells repolarized during the falling phase of the action potential waveform (Fig. 6D, bottom, black trace). Sodium conductance (Fig. 6D, bottom, red trace) was calculated and plotted as a function of stimulation number. $hNa_V1.8$ currents showed increasing levels of use-dependent inhibition as stimulation frequency increased for both vehicle-treated (Fig. 6E) and LTGO-33-treated cells (Fig. 6F), with LTGO-33-treated cells starting from a lower current level during the first pulse due to LTGO-33 inhibition.

Since recovery of conductance could be masked by use-dependent inhibition, we used a curve fitting approach to subtract the use-dependent inhibition effect (Fig. 6G). We applied a single-exponential fit to the data measured from vehicle-treated cells (filled black circles) to plot the time course of use-dependent inhibition. We then subtracted the values of the fitted line from the experimental data, which gave a residual response (open black circles; vehicle recovered) that represents the difference between the use-dependent inhibition effect (the fitted curve) and the measured vehicle data, in this case close to no residual response; this process removed the confounding effect of use-dependent inhibition. To quantitate reverse-use dependence in the LTGO-33-treated cells, we first had to remove the effect of use-dependent inhibition. For each cell, we used the single exponential fit parameters derived from the vehicle-treated data to generate a curve that would fit the LTGO-33-treated data (filled red circles). This required scaling the plateau parameter (a component of the exponential fit that describes the Y value extending to infinite times) to match the degree of inhibition. If conductance was inhibited to 60% of its starting value by 100 nM LTGO-33, then the plateau parameter would be multiplied by 0.6. Having thus scaled the single-exponential fit, we measured the residual difference between the expected course of use-dependent inhibition (the fitted curve) and the LTGO-33-treated experimental data (filled red circles). After we removed the use-dependent inhibition effect, we observed a small recovery of conductance in the LTGO-33-treated residual response (open red circles; LTGO-33 recovered), representing the reverse use-dependence effect.

Plotting the fraction of conductance recovered as a function of stimulation number yielded small increases in conductance at 10, 20, and 40 Hz during the first 10 stimulations that stabilized over the last 30 stimulations (Fig. 6H). Recovery was frequency dependent with 5% recovery at 10 Hz and 9% recovery at 20 and 40 Hz (Fig. 6I). No recovery was observed at 3 Hz or lower.

LTGO-33 Inhibits $Na_V1.8$ Variants Associated with Pain Disorders

Defining work that established a genetic role of $Na_V1.8$ in human pain biology uncovered multiple $Na_V1.8$ variants in patients with diverse pain phenotypes. The $hNa_V1.8$ gain of function mutations S242T associated with neuropathic pain in diabetic peripheral neuropathy (Han et al., 2018), L554P, A1304T, G1662S, and I1706V associated with painful small fiber neuropathy (Faber et al., 2012; Huang et al., 2013; Han et al., 2014; Duan et al., 2016a; Xiao et al., 2019), and the common single nucleotide polymorphism A1073V associated with higher thresholds for experimental mechanical pain, reduced post-operative abdominal pain, and increased analgesia success rate (Duan et al., 2018b; Coates et al., 2019; Karataş et al., 2023) were generated and evaluated in transiently expressing ND7/23 cells. The $hNa_V1.8$ clone used in

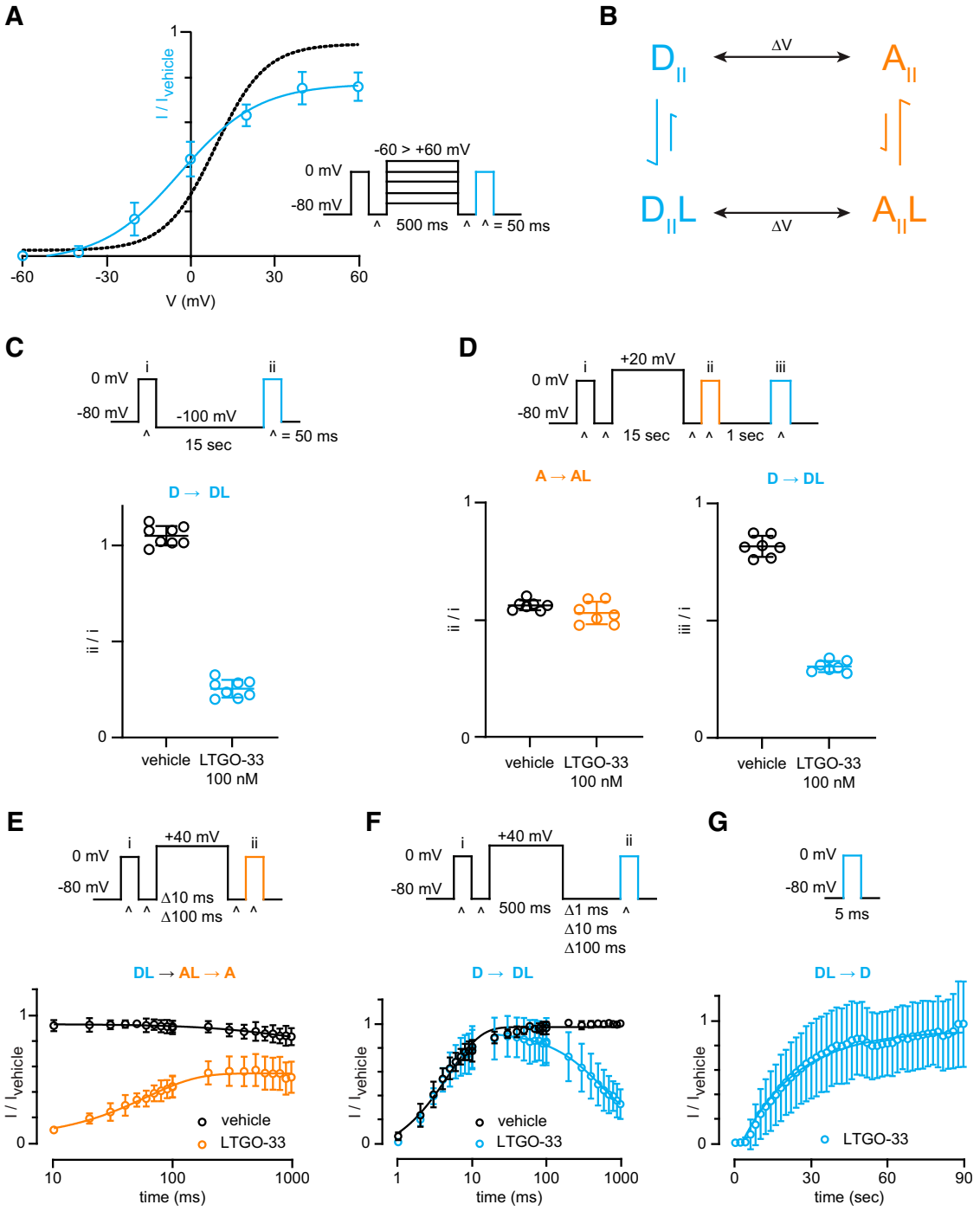

Fig. 5. Stabilization of the VSDII deactivated state by LTGO-33. (A) Voltage dependence of compound dissociation as measured by voltage clamp protocol on right. Blue indicates the fraction of recovered current relative to vehicle control before application of 100 nM LTGO-33. Uninhibited current following application of 100 nM LTGO-33 was subtracted to measure recovery of inhibited channels. Mean ± S.D. $n = 8$ cells. Black curve is Boltzmann fit of $hNa_V1.8$ HEK GV shown in Supplemental Fig. 1A, open black circles. (B) Conceptual model depicting transitions between the deactivated (D) and activated (A) VSDII, governed by voltage, and the apo- and ligand-bound (L) states, governed by LTGO-33 affinity. Blue indicates ligand-bound transitions of the deactivated state and orange indicates ligand-bound transitions for the activated state. (C) Fraction of current remaining after vehicle or 100 nM LTGO-33 application for 15 s at −100 mV (voltage protocol top). Ratio of peak ii to peak i in black for vehicle; ratio of peak ii to vehicle peak i is in blue for LTGO-33. Mean ± S.D. $n = 8$ cells. Arrow represents proposed state transition shown in (B). (D) Fraction of current remaining after vehicle or 100 nM LTGO-33 application for 15 s at +20 mV (voltage protocol top). Left, ratio of peak ii to peak i for vehicle and ratio of peak ii to vehicle peak i for LTGO-33. Right, ratio of peak iii to peak i for vehicle and ratio of peak iii to vehicle peak i for LTGO-33. Black is vehicle and blue/orange is LTGO-33. Mean ± S.D. $n = 7$ cells. Arrows represent proposed state transitions shown in (B). (E) Fraction of current recovered after steps to +40 mV for increasing durations (top, voltage protocol). Ratio of peak ii to peak i is plotted for vehicle (black), and ratio of peak ii to vehicle peak is plotted for 100 nM LTGO-33 (orange). Uninhibited current following application of 100 nM LTGO-33 was subtracted to measure recovery of inhibited channels. Orange line represents single-exponential fit to average LTGO-33 data. Mean ± S.D. $n = 6$ cells. Arrows represent proposed state transitions shown in (B). (F) Fraction of current remaining after 500 ms steps to +40 mV followed by recovery at −80 mV for increasing durations (top, voltage protocol). Ratio of peak ii to peak i is plotted for vehicle (black); ratio of peak ii to vehicle peak is plotted for 100 nM LTGO-33 (blue). Uninhibited current following application of 100 nM LTGO-33 was subtracted to

our experiments contained Val1073, which is present in nearly 40% of the population; therefore, this position was changed to Ala1073. These mutations are localized throughout the channel sequence, but none reside directly within the putative VSDII binding pocket (Fig. 7A). The potency of LTGO-33 on all channel variants was similar to WT $hNa_V1.8$ (Table 3), demonstrating that LTGO-33 can interdict the VSDII pocket of these channels to inhibit function (Fig. 7E).

Discussion

The results presented herein describe the pharmacology, interaction site, and mechanism of action of LTGO-33, a novel, potent, and selective $Na_V1.8$ inhibitor. Differentiated from prior published $Na_V1.8$ inhibitors, LTGO-33 showed no preference for inhibiting an inactivated state and mapped to a distinct binding site on VSDII (Jarvis et al., 2007; Kort et al., 2008; McGaraughty et al., 2008; Scanio et al., 2010; Zhang et al., 2010; Payne et al., 2015). Some $Na_V1.8$ inhibitors interact with inner S6 segments in the pore domain whereas LTGO-33 interacts with the extracellular cleft of VSDII to stabilize the deactivated state (Payne et al., 2015; Huang et al., 2022).

LTGO-33 inhibited native $Na_V1.8$ channels in both non-human primate and human DRG neurons but was much less effective in inhibiting native $Na_V1.8$ channels in dog, rat, and mouse DRG neurons. This species-specific pharmacology warrants caution when testing in rodent pain behavioral assays, as it may be challenging to obtain sufficient pharmacokinetic exposure levels to sufficiently engage $Na_V1.8$ channels in vivo to the extent required to impact analgesia (Qin et al., 2023). Translational models of target engagement using microneurography and thermal challenge assays in non-human primates have been used to evaluate $Na_V1.7$ inhibitors and represent potentially viable biomarkers to pursue for $Na_V1.8$ inhibitors (Pajouhesh et al., 2020; Kraus et al., 2021). In humans, a suite of thermal, mechanical, and electrical challenge models in healthy volunteers has been leveraged to evaluate target engagement with $Na_V1.8$ inhibitors in phase 1 studies (Hijma et al., 2021, 2022).

LTGO-33 suppressed action potential firing in cultured human DRG neurons in a frequency-dependent manner, consistent with the role of $Na_V1.8$ in sustaining high-frequency firing driven by the right-shifted voltage-dependence of inactivation coupled with rapid recovery from inactivation (Renganathan et al., 2001; Vijayaragavan et al., 2001; Han et al., 2015). These neurons express a mixture of TTX-S Na_V channels, including $Na_V1.6$ and $Na_V1.7$, along with the TTX-R Na_V channels $Na_V1.8$ and $Na_V1.9$ (Alexandrou et al., 2016; Zhang et al., 2017). The specific functional contribution of individual Na_V isoforms to action potential firing likely varies between individual neurons with a continuum of $Na_V1.8$ functional expression profiles present. Accordingly, neurons exhibiting less inhibition of action potential firing by LTGO-33 may express less $Na_V1.8$ and more $Na_V1.7$ at the plasma membrane. Conversely, neurons exhibiting near full block of action potential firing by LTGO-33 may predominantly express $Na_V1.8$.

Chimeras between $hNa_V1.8$ and $rNa_V1.8$, which was not potently inhibited by LTGO-33, identified VSDII as the critical domain required for compound inhibition. Small twofold differences in the potency of LTGO-33 against the rat–human VSDII chimera compared with WT $hNa_V1.8$ indicate potential expression system differences between HEK293 and ND7/23 cells and/or minor contributions from regions residing outside VSDII. Through prosecution of a minimal gain of function chimera, reversion constructs, and a detailed site-directed mutagenesis campaign spanning the VSDII region, we mapped the site required for LTGO-33 inhibition to the VSDII extracellular cleft. Alanine mutations with the greatest loss of LTGO-33 potency were found on the S1, S3, and S4 helices as well as the S3–S4 linker, suggesting the involvement of each of these segments in forming components of the LTGO-33 binding pocket.

By comparing $hNa_V1.8$ VSDII residues most important for LTGO-33 inhibition, marked by fivefold or greater loss in potency in site-directed mutagenesis studies, across the human Na_V family, the S3–S4 loop region emerged as an area of poor conservation that likely drove the high degree of isoform selectivity observed. Leu744 and Leu752 are conserved between $Na_V1.1$–$Na_V1.9$ indicating these hydrophobic residues are important for LTGO-33 inhibition but not selectivity. Val746 is a hydrophobic Leu in other Na_V channels and may contribute to selectivity. The basic and charged Lys749 is a hydrophobic Val in all other sodium channels except for $Na_V1.5$ where it is a Met. The small and flexible Gly750 is a polar Glu, Ser, or Gln in all other Na_V channels. We propose that Lys749 and Gly750, positioned in the extracellular S3–S4 loop region, are critical amino acids for imparting robust $Na_V1.8$ selectivity. Lys748, which is a charged/polar Asp or Asn in most other channels, may also play an important role in selectivity that was not uncovered in our alanine scan approach. Inspection of the $hNa_V1.8$ VSDII S3-S4 loop comprising LGVAKKGSLSV reveals a di-basic core comprised of Lys748 and Lys749 surrounded on either side by smaller and hydrophobic amino acids. Interdicting this novel small molecule site on VSDII may afford a greater degree of isoform selectivity, and therefore margin for safety for analgesic drug development, than molecules that target either the pore region or local anesthetic site that are both highly conserved between family members.

The spider venom toxin ProTx-II interacts with a LFLAD sequence in $Na_V1.7$ VSDII S3–S4 (Xu et al., 2019). In $Na_V1.8$ the corresponding amino acids of this site are LGVAK. L744A and V746A were among the most impactful mutations resulting in loss of LTGO-33 potency on $Na_V1.8$, suggesting a partially overlapping three-dimensional binding region with ProTx-II may exist. Electrostatic repulsion by basic residues in ProTx-II inserted into the VSD could partially oppose movement of the R1 gating charge and/or electrostatically

measure recovery of inhibited channels. Black line is single-exponential fit to vehicle data. Blue line represents single-exponential fit to average of LTGO-33 data from 20 ms to 1000 ms. Mean ± S.D. $n = 6$ cells. Arrow represents proposed state transition shown in (B). (G) Fraction of current recovered after 5 ms steps to +20 mV during 100 nM LTGO-33 washout with vehicle (top, voltage protocol). Blue symbols represent ratio of measured current to vehicle preceding initial application of LTGO-33. Uninhibited current following application of 100 nM LTGO-33 was subtracted to measure recovery of inhibited channels. Blue line represents single-exponential fit to average data. Mean ± S.D. $n = 8$ cells. Arrow represents proposed state transition shown in (B).

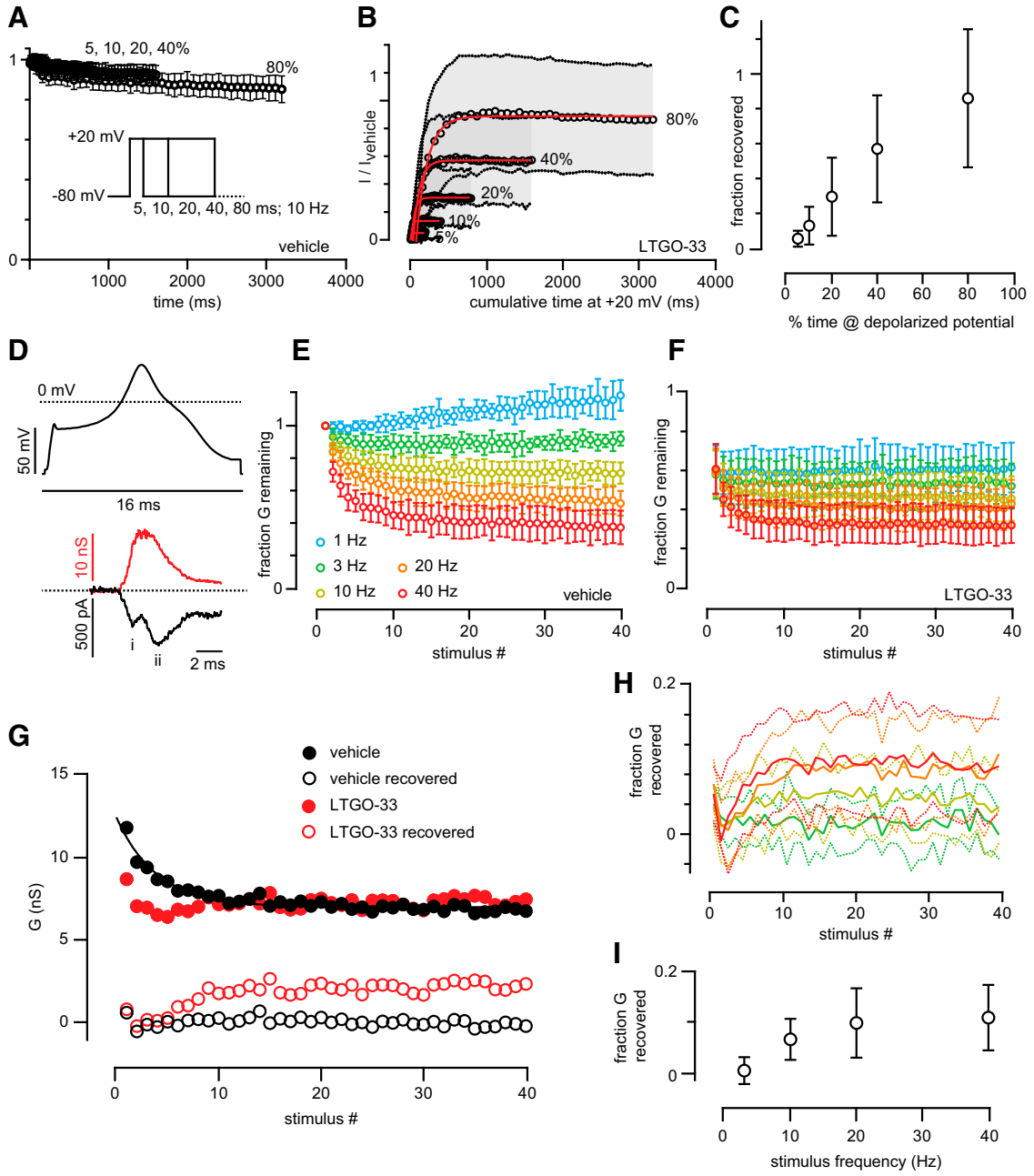

Fig. 6. Recovery from inhibition by high frequency depolarizations. (A) Remaining current in vehicle-treated ND7/23 cells after 40 pulses to +20 mV for 5, 10, 20, 40, or 80 ms with an intersweep interval of 100 ms (10 Hz); protocol shown in inset. Percent time of sweep at +20 mV is indicated. X-axis indicates cumulative time at +20 mV. Mean ± S.D. $n = 7$. (B) Recovered current in HEK293 cells stably expressing $hNa_V1.8$ treated with 100 nM LTGO-33 after 40 pulses to +20 mV for 5, 10, 20, 40, or 80 ms with intersweep interval of 100 ms (10 Hz) using voltage protocol inset in Fig. 6A. Data points represent fraction of current recovered relative to vehicle. Uninhibited current following application of 100 nM LTGO-33 was subtracted to measure recovery of inhibited channels. Percent time of sweep at +20 mV is indicated. Red line is single-exponential fit to average data. X-axis indicates cumulative time at +20 mV. Mean ± S.D. $n = 7$. (C) Fraction of current recovered plotted relative to percent time of sweep at +20 mV. Fraction of current derived from plateau of single-exponential fits in Fig. 6B. Mean ± S.D. (D) DRG action potential, obtained from a small diameter rat DRG neuron, used to stimulate $hNa_V1.8$ expressed in ND7/23 cells (top). Current in black and calculated conductance in red shown for a representative cell (bottom). (E) Fraction conductance (G) remaining after 40 stimulations with an AP waveform at 1, 3, 10, 20, or 40 Hz in ND7/23 cells transfected with $hNa_V1.8$ treated with vehicle (0.1% DMSO). Mean ± S.D. $n = 8$. (F) Fraction conductance remaining after 40 stimulations with an AP waveform at 1, 3, 10, 20, or 40 Hz in ND7/23 cells treated with 100 nM LTGO-33, normalized to starting conductance in vehicle-treated cells. Mean ± S.D. $n = 8$. (G) Example analysis to subtract use-dependent inhibition from recovered conductance. Filled black circles represent the conductance of a vehicle-treated ND7/23 cell in response to 40 sweeps of the AP waveform in Fig. 6D and filled red circles the same cell treated with 100 nM LTGO-33. Open black circles are the recovered conductance of a single-exponential fit to the filled black circles. Open red circles are the recovered conductance from a single-exponential fit to filled red circles using the rate constant (K) from vehicle fit and scaled plateau. (H) Fraction of conductance recovered after 100 nM LTGO-33 treatment at each frequency, normalized to the starting conductance in vehicle. Colors correspond to the frequencies indicated in panel E. Thick line depicts mean, dotted lines depict S.D. $n = 8$. (I) Fraction conductance recovered at each frequency. Fraction recovered is derived from plateau of single-exponential fit to curves in panel H. Mean ± S.D.

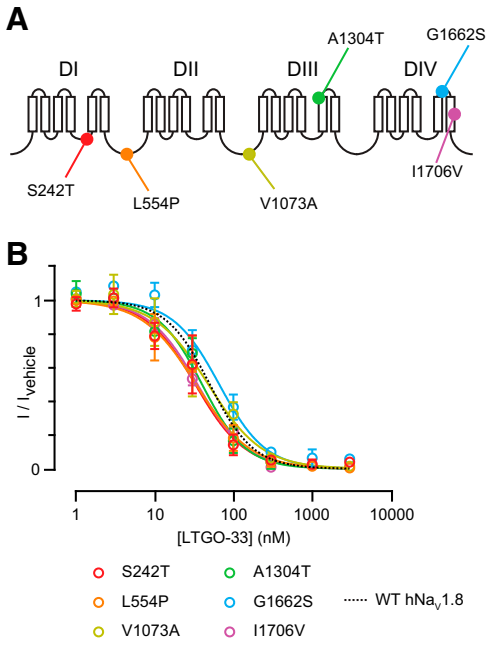

Fig. 7. LTGO-33 inhibition of $Na_V1.8$ variants associated with human pain disorders. (A) Locations of $hNa_V1.8$ variants, indicated by colored circles, within channel topology. (B) Potency of LTGO-33 on $hNa_V1.8$ variants. Dotted black line indicates LTGO-33 IC_{50} on $hNa_V1.8$ in ND7/23 cells taken from Fig. 4D. Mean ± S.D. $n = 6$ cells for each concentration.

modulate acidic residues that favor gating charge movement. Similarly, the μO-conotoxin MrVIA inhibited $Na_V1.4$ by interaction with VSDII, and neutralization of the DII R1 and R2 gating charges prolonged toxin inhibition (Leipold et al., 2007). Our observation that mutation of R756Q reduced LTGO-33 potency suggests the compound may inhibit channel function, in part, by opposing the first gating charge movement, thus stabilizing the deactivated state of VSDII.

Sulfonamide-based inhibitors that directly engage the R4 gating charge in VSDIV of $Na_V1.7$ penetrate deeper in the membrane compared with LTGO-33 and yield a 3,000-fold loss in potency upon mutation (Ahuja et al., 2015). The smaller fivefold potency loss of LTGO-33 with the R756Q gating charge mutation suggests stabilization of deactivated VSDII is mediated through additional amino acids in the S3–S4 linker. Our alanine scan did not encompass the entire VSDII sequence; therefore, it is possible that other residues important for LTGO-33 interaction, including those within the S1–S2 region, exist that were not evaluated in our mutagenesis campaign. A structural biology approach would be required to elucidate an exact binding pocket with resolution of key $Na_V1.8$ amino acid side changes forming chemical bonds with LTGO-33 atoms.

It may be challenging to leverage docking of molecules to the LTGO-33 site in VSDII using the published $Na_V1.8$ cryo-EM structure (Huang et al., 2022). Most Na_V structures reflect VSDs in their activated state, given the absence of a membrane potential in preparations of purified protein used for structural studies. The native conformation of VSDII in the deactivated state, where LTGO-33 interaction is robust, may be structurally distinct from VSDII in the activated state or LTGO-33 may bind a cryptic pocket not readily discernable in an apo-structure and subsequently undergo an induced fit. Solving the structure of $Na_V1.8$ with deactivated VSDII would shed light on these points.

Biophysical mechanism of action studies demonstrated that LTGO-33 stabilized the deactivated state of VSDII, effectively keeping the channel closed by preventing movement of VSDII. The compound can be displaced from $Na_V1.8$ by depolarization to positive potentials to promote transition of VSDII to the activated state from which the compound dissociates from the binding pocket. While our experiments point to modulation of VSDII gating charge movement as the driver for channel inhibition, voltage-clamp fluorometry studies would be required to directly demonstrate block of VSDII movement to the activated state following LTGO-33 challenge and recovery of VSDII movement coupled with ligand displacement during sustained depolarization.

Using an action potential waveform presented at various frequencies, reverse use dependence was not readily observed with 100 nM LTGO-33 until frequencies reached 20 to 40 Hz in which channels were depolarized over 0 mV for 10% to 20% of the total recording period. Reverse use dependence would be expected to be contingent on compound concentration, with higher concentrations further blunting any effect as channels are driven to higher levels of target occupancy. Although reverse-use dependence was discernable, the magnitude was small and comprised 5% to 10% of total conductance at higher frequencies. Given human nociceptive C-fibers expressing $Na_V1.8$ in situ generally fire action potentials in the 0.4 to 10 Hz range following thermal, mechanical, and chemical algogenic stimuli, it is unlikely that LTGO-33 receptor occupancy at VSDII would be meaningfully and negatively impacted at physiologically relevant spiking rates (Van Hees and Gybels, 1981; LaMotte et al., 1984; Torebjörk et al., 1984; Campero et al., 2001).

Rare gain of function $Na_V1.8$ variants have been identified in humans with painful neuropathies including diabetic peripheral neuropathy (Han et al., 2018) and small fiber neuropathy (Faber et al., 2012; Huang et al., 2013; Han et al., 2014; Duan et al., 2016a; Xiao et al., 2019). LTGO-33 was able to effectively block these $Na_V1.8$ variants with potencies similar to WT $hNa_V1.8$ channels. Selective inhibition of $Na_V1.8$ may not only provide analgesia in the general population afflicted with acute and chronic pain disorders but additionally in humans with hyperactive variants in cases of genetically driven pain.

TABLE 3

IC_{50} values for $hNa_V1.8$ variants associated with human pain disorders

Channels transiently expressed in ND7/23 cells were tested using manual patch clamp electrophysiology.

Construct	IC_{50} (nM)	95% CI (nM)	n (cells used for IC_{50})
WT (from Table 2)	50	36 – 69	6
S242T	33	27 – 40	6
L554P	34	28 – 41	6
V1073A	48	36 – 63	6
A1304T	40	32 – 49	5
G1662S	66	53 – 82	6
I1706V	35	32 – 38	6

Acknowledgments

The authors would like to thank Shanti Amagasu for thoughtful conversations and critical reading of the manuscript, Tina Holt for testing purity of compounds, and Kevin Carlin and Tamara Cotta for help procuring data files.

Data Availability

The data that support the findings of this study are available upon request from the corresponding author.

Authorship Contributions

Participated in research design: Gilchrist, Yang, Moyer.

Conducted experiments: Gilchrist, Yang, Jiang.

Performed data analysis: Gilchrist, Yang, Jiang, Moyer.

Wrote or contributed to the writing of the manuscript: Gilchrist, Moyer.

References

Ahern CA, Payandeh J, Bosmans F, and Chanda B (2016) The hitchhiker's guide to the voltage-gated sodium channel galaxy. *J Gen Physiol* **147:**1–24.

Ahuja S, Mukund S, Deng L, Khakh K, Chang E, Ho H, Shriver S, Young C, Lin Jr S, Johnson Jr JP, et al. (2015) Structural basis of Nav1.7 inhibition by an isoform-selective small-molecule antagonist. *Science* **350:**aac5464.

Alexandrou AJ, Brown AR, Chapman ML, Estacion M, Turner J, Mis MA, Wilbrey A, Payne EC, Gutteridge A, Cox PJ, et al. (2016) Subtype-selective small molecule inhibitors reveal a fundamental role for Nav1.7 in nociceptor electrogenesis, axonal conduction and presynaptic release. *PLoS One* **11:**e0152405.

Basbaum AI, Bautista DM, Scherrer G, and Julius D (2009) Cellular and molecular mechanisms of pain. *Cell* **139:**267–284.

Bennett DL, Clark AJ, Huang J, Waxman SG, and Dib-Hajj SD (2019) The role of voltage-gated sodium channels in pain signaling. *Physiol Rev* **99:**1079–1151.

Blair NT and Bean BP (2002) Roles of tetrodotoxin (TTX)-sensitive Na+ current, TTX-resistant Na+ current, and Ca2+ current in the action potentials of nociceptive sensory neurons. *J Neurosci* **22:**10277–10290.

Bosmans F, Martin-Eauclaire M-F, and Swartz KJ (2008) Deconstructing voltage sensor function and pharmacology in sodium channels. *Nature* **456:**202–208.

Browne LE, Clare JJ, and Wray D (2009) Functional and pharmacological properties of human and rat NaV1.8 channels. *Neuropharmacology* **56:**905–914.

Campero M, Serra J, Bostock H, and Ochoa JL (2001) Slowly conducting afferents activated by innocuous low temperature in human skin. *J Physiol* **535:**855–865.

Catterall WA (2000) From ionic currents to molecular mechanisms: the structure and function of voltage-gated sodium channels. *Neuron* **26:**13–25.

Coates MD, Kim JS, Carkaci-Salli N, Vrana KE, Koltun WA, Puhl HL, Adhikary SD, Janicki PK, and Ruiz-Velasco V (2019) Impact of the $Na_V1.8$ variant, A1073V, on post-sigmoidectomy pain and electrophysiological function in rat sympathetic neurons. *J Neurophysiol* **122:**2591–2600.

Davidson S, Copits BA, Zhang J, Page G, Ghetti A, and Gereau 4th RW (2014) Human sensory neurons: membrane properties and sensitization by inflammatory mediators. *Pain* **155:**1861–1870.

Duan G, Han C, Wang Q, Guo S, Zhang Y, Ying Y, Huang P, Zhang L, Macala L, Shah P, et al. (2016a) A SCN10A SNP biases human pain sensitivity. *Mol Pain* **12:**1744806916666083.

Duan G, Sun J, Li N, Zheng H, Guo S, Zhang Y, Wang Q, Ying Y, Zhang M, Huang P, et al. (2018) A variant in the SCN10A enhancer may affect human mechanical pain sensitivity. *Mol Pain* **14:**1744806918763275.

Edgerton GB, Blumenthal KM, and Hanck DA (2008) Evidence for multiple effects of ProTxII on activation gating in Na(V)1.5. *Toxicon* **52:**489–500.

Faber CG, Lauria G, Merkies ISJ, Cheng X, Han C, Ahn H-S, Persson A-K, Hoeijmakers JGJ, Gerrits MM, Pierro T, et al. (2012) Gain-of-function Nav1.8 mutations in painful neuropathy. *Proc Natl Acad Sci USA* **109:**19444–19449.

Finnerup NB, Attal N, Haroutounian S, McNicol E, Baron R, Dworkin RH, Gilron I, Haanpää M, Hansson P, Jensen TS, et al. (2015) Pharmacotherapy for neuropathic pain in adults: a systematic review and meta-analysis. *Lancet Neurol* **14:**162–173.

Gerhauser I, Hahn K, Baumgärtner W, and Wewetzer K (2012) Culturing adult canine sensory neurons to optimise neural repair. *Vet Rec* **170:**102.

Gonzalez-Lopez E, Imamura Kawasawa Y, Walter V, Zhang L, Koltun WA, Huang X, Vrana KE, and Coates MD (2018) Homozygosity for the SCN10A polymorphism rs6795970 is associated with hypoalgesic inflammatory bowel disease phenotype. *Front Med (Lausanne)* **5:**324.

Han C, Estacion M, Huang J, Vasylyev D, Zhao P, Dib-Hajj SD, and Waxman SG (2015) Human Na(v)1.8: enhanced persistent and ramp currents contribute to distinct firing properties of human DRG neurons. *J Neurophysiol* **113:**3172–3185.

Han C, Huang J, and Waxman SG (2016) Sodium channel Nav1.8: emerging links to human disease. *Neurology* **86:**473–483.

Han C, Themistocleous AC, Estacion M, Dib-Hajj FB, Blesneac I, Macala L, Fratter C, Bennett DL, Waxman SG, and Dib-Hajj SD (2018) The novel activity of carbamazepine as an activation modulator extends from NaV1.7 mutations to the NaV1.8-S242T mutant channel from a patient with painful diabetic neuropathy. *Mol Pharmacol* **94:** 1256–1269.

Han C, Vasylyev D, Macala LJ, Gerrits MM, Hoeijmakers JGJ, Bekelaar KJ, Dib-Hajj SD, Faber CG, Merkies ISJ, and Waxman SG (2014) The G1662S NaV1.8 mutation in small fibre neuropathy: impaired inactivation underlying DRG neuron hyperexcitability. *J Neurol Neurosurg Psychiatry* **85:**499–505.

Hijma HJ, Siebenga PS, Kam ML de, and Groeneveld GJ (2021) A phase 1, randomized, double-blind, placebo-controlled, crossover study to evaluate the pharmacodynamic effects of VX-150, a highly selective NaV1.8 inhibitor, in healthy male adults. *Pain Med* **22:**1814–1826.

Hijma HJ, Brummelen EMJ, Siebenga PS, and Groeneveld GJ (2022) A phase I, randomized, double-blind, placebo-controlled, single- and multiple dose escalation study evaluating the safety, pharmacokinetics and pharmacodynamics of VX-128, a highly selective Nav1.8 inhibitor, in healthy adults. *Clin Transl Sci* **15:**981–993.

Holmes D (2016) The pain drain. *Nature* **535**:S2–S3.

Huang J, Yang Y, Zhao P, Gerrits MM, Hoeijmakers JGJ, Bekelaar K, Merkies ISJ, Faber CG, Dib-Hajj SD, and Waxman SG (2013) Small-fiber neuropathy Nav1.8 mutation shifts activation to hyperpolarized potentials and increases excitability of dorsal root ganglion neurons. *J Neurosci* **33:**14087–14097.

Huang X, Jin X, Huang G, Huang J, Wu T, Li Z, Chen J, Kong F, Pan X, and Yan N (2022) Structural basis for high-voltage activation and subtype-specific inhibition of human $Na_V1.8$. *Proc Natl Acad Sci USA* **119:**e2208211119.

Huang Y, Poslusney M, Ernst G, and Barrow J (2020) inventors, Pyridine carboxamide compounds for inhibiting Nav1.8. WO 2020/014246 Al. 2020 Jan 16.

Jarvis MF, Honore P, Shieh C-C, Chapman M, Joshi S, Zhang X-F, Kort M, Carroll W, Marron B, Atkinson R, et al. (2007) A-803467, a potent and selective Nav1.8 sodium channel blocker, attenuates neuropathic and inflammatory pain in the rat. *Proc Natl Acad Sci USA* **104:**8520–8525.

Jo S, Zhang HB, and Bean BP (2023) Use-dependent relief of inhibition of Nav1.8 channels by A-887826. *Mol Pharmacol* **103:**221–229.

Jones J, Correll DJ, Lechner SM, Jazic I, Miao X, Shaw D, Simard C, Osteen JD, Hare B, Beaton A, et al.; VX21-548-101 and VX21-548-102 Trial Groups (2023) Selective inhibition of $Na_V1.8$ with VX-548 for acute pain. *N Engl J Med* **389:**393–405.

Karataş E, Sümbüllü M, Kahraman ÇY, and Çakmak FA (2023) Association between single-nucleotide polymorphisms in candidate genes and success of pulpal anesthesia after inferior alveolar nerve block. *J Endod* **49:**18–25.

Knezevic NN, Cicmil N, Knezevic I, and Candido KD (2015) Discontinued neuropathic pain therapy between 2009-2015. *Expert Opin Investig Drugs* **24:**1631–1646.

Kort ME, Drizin I, Gregg RJ, Scanio MJC, Shi L, Gross MF, Atkinson RN, Johnson MS, Pacofsky GJ, Thomas JB, et al. (2008) Discovery and biological evaluation of 5-aryl-2-furfuramides, potent and selective blockers of the Nav1.8 sodium channel with efficacy in models of neuropathic and inflammatory pain. *J Med Chem* **51:**407–416.

Kraus RL, Zhao F, Pall PS, Zhou D, Vardigan JD, Danziger A, Li Y, Daley C, Ballard JE, Clements MK, et al. (2021) $Na_v1.7$ target modulation and efficacy can be measured in nonhuman primate assays. *Sci Transl Med* **13:**eaay1050.

LaMotte RH, Torebjörk HE, Robinson CJ, and Thalhammer JG (1984) Time-intensity profiles of cutaneous pain in normal and hyperalgesic skin: a comparison with C-fiber nociceptor activities in monkey and human. *J Neurophysiol* **51:**1434–1450.

Leipold E, DeBie H, Zorn S, Borges A, Olivera BM, Terlau H, and Heinemann SH (2007) muO conotoxins inhibit NaV channels by interfering with their voltage sensors in domain-2. *Channels (Austin)* **1:**253–262.

Lucas JW, Connor EM, and Bose J (2021) Back, lower limb, and upper limb pain among U.S. adults, 2019. *NCHS Data Brief* **415**:1–8.

Mäntyselkä P, Kumpusalo E, Ahonen R, Kumpusalo A, Kauhanen J, Viinamäki H, Halonen P, and Takala J (2001) Pain as a reason to visit the doctor: a study in Finnish primary health care. *Pain* **89:**175–180.

McGaraughty S, Chu KL, Scanio MJC, Kort ME, Faltynek CR, and Jarvis MF (2008) A selective Nav1.8 sodium channel blocker, A-803467 [5-(4-chlorophenyl-N-(3,5-dimethoxyphenyl)furan-2-carboxamide], attenuates spinal neuronal activity in neuropathic rats. *J Pharmacol Exp Ther* **324:**1204–1211.

Moyer BD, Murray JK, Ligutti J, Andrews K, Favreau P, Jordan JB, Lee JH, Liu D, Long J, Sham K, et al. (2018) Pharmacological characterization of potent and selective NaV1.7 inhibitors engineered from Chilobrachys jingzhao tarantula venom peptide JzTx-V. *PLoS One* **13:**e0196791.

Nahin RL (2015) Estimates of pain prevalence and severity in adults: United States, 2012. *J Pain* **16:**769–780.

Pajouhesh H, Beckley JT, Delwig A, Hajare HS, Luu G, Monteleone D, Zhou X, Ligutti J, Amagasu S, Moyer BD, et al. (2020) Discovery of a selective, state-independent inhibitor of $Na_V1.7$ by modification of guanidinium toxins. *Sci Rep* **10:**14791.

Payne CE, Brown AR, Theile JW, Loucif AJC, Alexandrou AJ, Fuller MD, Mahoney JH, Antonio BM, Gerlach AC, Printzenhoff DM, et al. (2015) A novel selective and orally bioavailable Nav 1.8 channel blocker, PF-01247324, attenuates nociception and sensory neuron excitability. *Br J Pharmacol* **172:**2654–2670.

Qin H, Wei A, Wang Y, Wang L, Xu H, Zhan Y, Tian X, Zheng Y, Gao Z, and Hu Y (2023) Discovery of selective $Na_V1.8$ inhibitors based on 5-chloro-2-(4,4-difluoroazepan-1-yl)-6-methyl nicotinamide scaffold for the treatment of pain. *Eur J Med Chem* **254:**115371.

Renganathan M, Cummins TR, and Waxman SG (2001) Contribution of Na(v)1.8 sodium channels to action potential electrogenesis in DRG neurons. *J Neurophysiol* **86:**629–640.

Scanio MJC, Shi L, Drizin I, Gregg RJ, Atkinson RN, Thomas JB, Johnson MS, Chapman ML, Liu D, Krambis MJ, et al. (2010) Discovery and biological evaluation of potent, selective, orally bioavailable, pyrazine-based blockers of the Na(v)1.8 sodium channel with efficacy in a model of neuropathic pain. *Bioorg Med Chem* **18:**7816–7825.

Schwarz S, Lehmbecker A, Tongtako W, Hahn K, Wang Y, Felmy F, Zdora I, Brogden G, Branitzki-Heinemann K, von Köckritz-Blickwede M, et al. (2020) Neurotrophic effects of G_{M1} ganglioside, NGF, and FGF2 on canine dorsal root ganglia neurons in vitro. *Sci Rep* **10:**5380.

Shiers S, Klein RM, and Price TJ (2020) Quantitative differences in neuronal subpopulations between mouse and human dorsal root ganglia demonstrated with RNAscope in situ hybridization. *Pain* **161:**2410–2424.

Silva JR and Goldstein SAN (2013) Voltage-sensor movements describe slow inactivation of voltage-gated sodium channels I: wild-type skeletal muscle Na(V)1.4. *J Gen Physiol* **141:**309–321.

Sokolov S, Kraus RL, Scheuer T, and Catterall WA (2008) Inhibition of sodium channel gating by trapping the domain II voltage sensor with protoxin II. *Mol Pharmacol* **73:**1020–1028.

Stefano GD, Yuan J-H, Cruccu G, Waxman SG, Dib-Hajj SD, and Truini A (2020) Familial trigeminal neuralgia—a systematic clinical study with a genomic screen of the neuronal electrogenisome. *Cephalalgia* **40:** 767–777.

Tongtako W, Lehmbecker A, Wang Y, Hahn K, Baumgärtner W, and Gerhauser I (2017) Canine dorsal root ganglia satellite glial cells represent an exceptional cell population with astrocytic and oligodendrocytic properties. *Sci Rep* **7:**13915.

Torebjörk HE, LaMotte RH, and Robinson CJ (1984) Peripheral neural correlates of magnitude of cutaneous pain and hyperalgesia: simultaneous recordings in humans of sensory judgments of pain and evoked responses in nociceptors with C-fibers. *J Neurophysiol* **51:**325–339.

Treede R-D, Rief W, Barke A, Aziz Q, Bennett MI, Benoliel R, Cohen M, Evers S, Finnerup NB, First MB, et al. (2015) A classification of chronic pain for ICD-11. *Pain* **156:**1003–1007.

Valtcheva MV, Copits BA, Davidson S, Sheahan TD, Pullen MY, McCall JG, Dikranian K, and Gereau 4th RW (2016) Surgical extraction of human dorsal root ganglia from organ donors and preparation of primary sensory neuron cultures. *Nat Protoc* **11:** 1877–1888.

Van Hees J and Gybels J (1981) C nociceptor activity in human nerve during painful and non painful skin stimulation. *J Neurol Neurosurg Psychiatry* **44:**600–607.

Varga Z, Zhu W, Schubert AR, Pardieck JL, Krumholz A, Hsu EJ, Zaydman MA, Cui J, and Silva JR (2015) Direct measurement of cardiac Na+ channel conformations reveals molecular pathologies of inherited mutations. *Circ Arrhythm Electrophysiol* **8:**1228–1239.

Vijayaragavan K, O'Leary ME, and Chahine M (2001) Gating properties of Na(v)1.7 and Na(v)1.8 peripheral nerve sodium channels. *J Neurosci* **21:**7909–7918.

Xiao Y, Barbosa C, Pei Z, Xie W, Strong JA, Zhang J-M, and Cummins TR (2019) Increased resurgent sodium currents in Nav1.8 contribute to nociceptive sensory neuron hyperexcitability associated with peripheral neuropathies. *J Neurosci* **39:**1539–1550.

Xu H, Li T, Rohou A, Arthur CP, Tzakoniati F, Wong E, Estevez A, Kugel C, Franke Y, Chen J, et al. (2019) Structural basis of Nav1.7 inhibition by a gating-modifier spider toxin. *Cell* **176:**702–715.e14.

Zhang X, Priest BT, Belfer I, and Gold MS (2017) Voltage-gated Na^+ currents in human dorsal root ganglion neurons. *eLife* **6:**e23235.

Zhang X-F, Shieh C-C, Chapman ML, Matulenko MA, Hakeem AH, Atkinson RN, Kort ME, Marron BE, Joshi S, Honore P, et al. (2010) A-887826 is a structurally novel, potent and voltage-dependent Na(v)1.8 sodium channel blocker that attenuates neuropathic tactile allodynia in rats. *Neuropharmacology* **59:**201–207.

Address correspondence to: John M. Gilchrist, Latigo Biotherapeutics, Inc., 1300 Rancho Conejo Blvd., Suite 305, Thousand Oaks, CA 91320. E-mail: jgilchrist@latigobio.com

Molecular Pharmacology

MOLPHARM-AR-2023-000789

Supplemental Data

Pharmacologic Characterization of LTGO-33, a Selective Small Molecule Inhibitor of the Voltage-Gated Sodium Channel $Na_V1.8$ with a Unique Mechanism of Action

John M. Gilchrist, Nien-Du Yang, Victoria Jiang, and Bryan D. Moyer

Latigo Biotherapeutics Inc., 1300 Rancho Conejo Blvd Suite 305, Thousand Oaks CA 91320

Figure S1

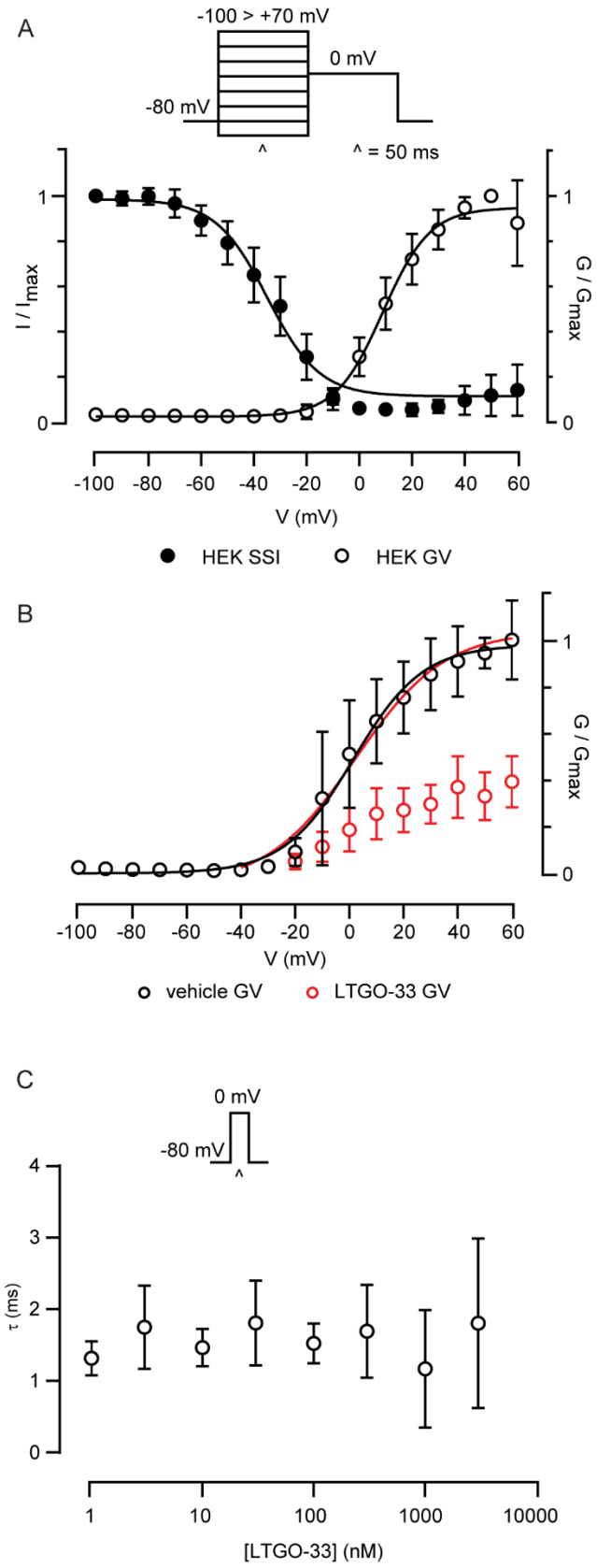

Supplemental Figure 1. Conductance-voltage and inactivation-voltage relationships for hNa$_V$1.8 in HEK293 cells.

A) Conductance-voltage (GV) and steady-state inactivation (SSI) relationships measured with voltage protocol (top). Filled circles represent SSI and open circles represent GV. Mean ± SD. n = 10 cells.

B) Conductance-voltage relationship measured with voltage protocol in A. Circles represent GV before (black) and after (red) treatment with 100 nM LTGO-33, normalized to the peak conductance in vehicle period. Black curve depicts a Boltzmann fit to the black circles ($V_{1/2}$ = 1.5 mV, 95% CI: -1.6 to 4.8 mV, n = 8 cells). Red curve is a Boltzmann fit to the post-treatment GV ($V_{1/2}$ = 2.3 mV, 95% CI: -4.3 to 7.2 mV, n = 8 cells), normalized to LTGO-33-treated cells.

C) Rate of fast inactivation versus applied concentration of LTGO-33. Rate is the tau of a single-exponential fit to the decay phase of inactivating Na$_V$ current during measurement of IC_{50} shown in Fig 1b (resting state, black). Mean ± SD. n = 5 cells per concentration.

Figure S2

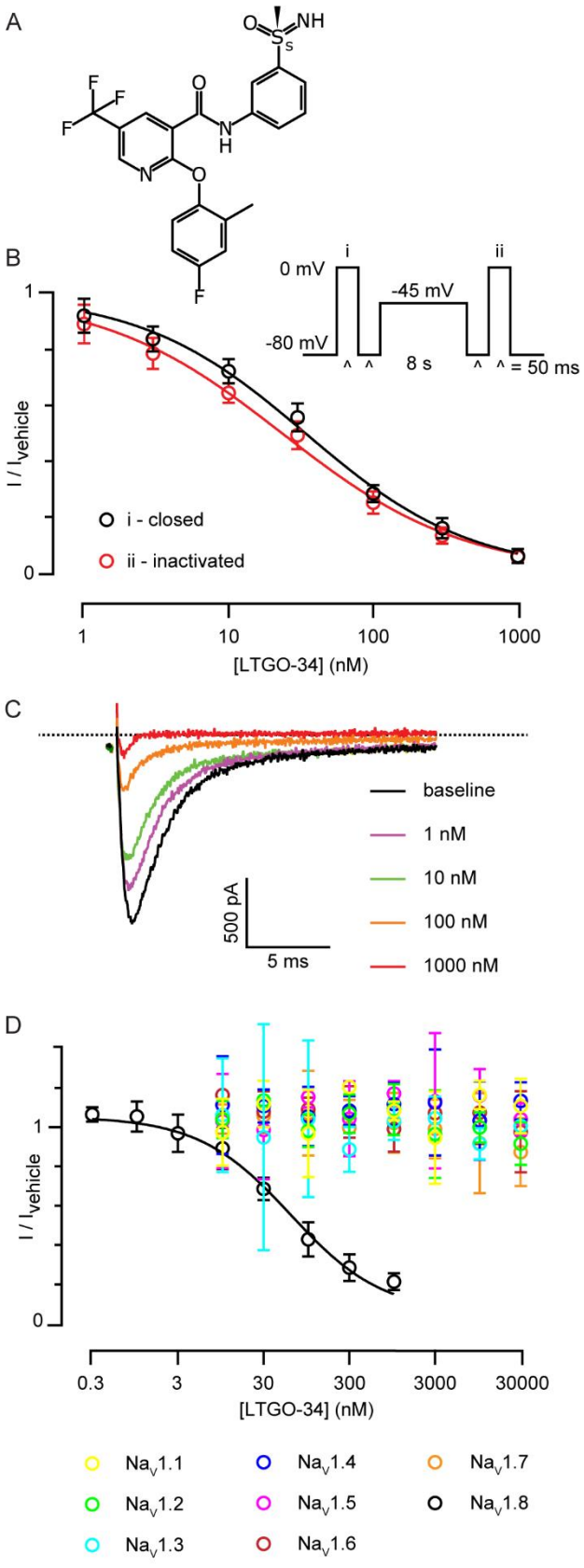

Supplemental Figure 2. LTGO-34 potently and selectively inhibits $Na_V1.8$.

A) Structure of LTGO-34

B) Voltage protocol (top) used to generate concentration-response curves for LTGO-34 (bottom) on h$Na_V1.8$ stable cell line. Black shows inhibition of closed or resting channels and red shows inhibition following channel entry into inactivated states. Mean ± SD. n = 7 cells per concentration.

C) Example traces of $Na_V1.8$ inhibition by escalating concentrations of LTGO-34. Currents elicited by 50 ms pulse to 0 mV from a holding potential of -80 mV.

D) LTGO-34 potency against other human Na_V isoforms. Mean ± SD. n = 2-8 wells per concentration (Table S5).

Figure S3

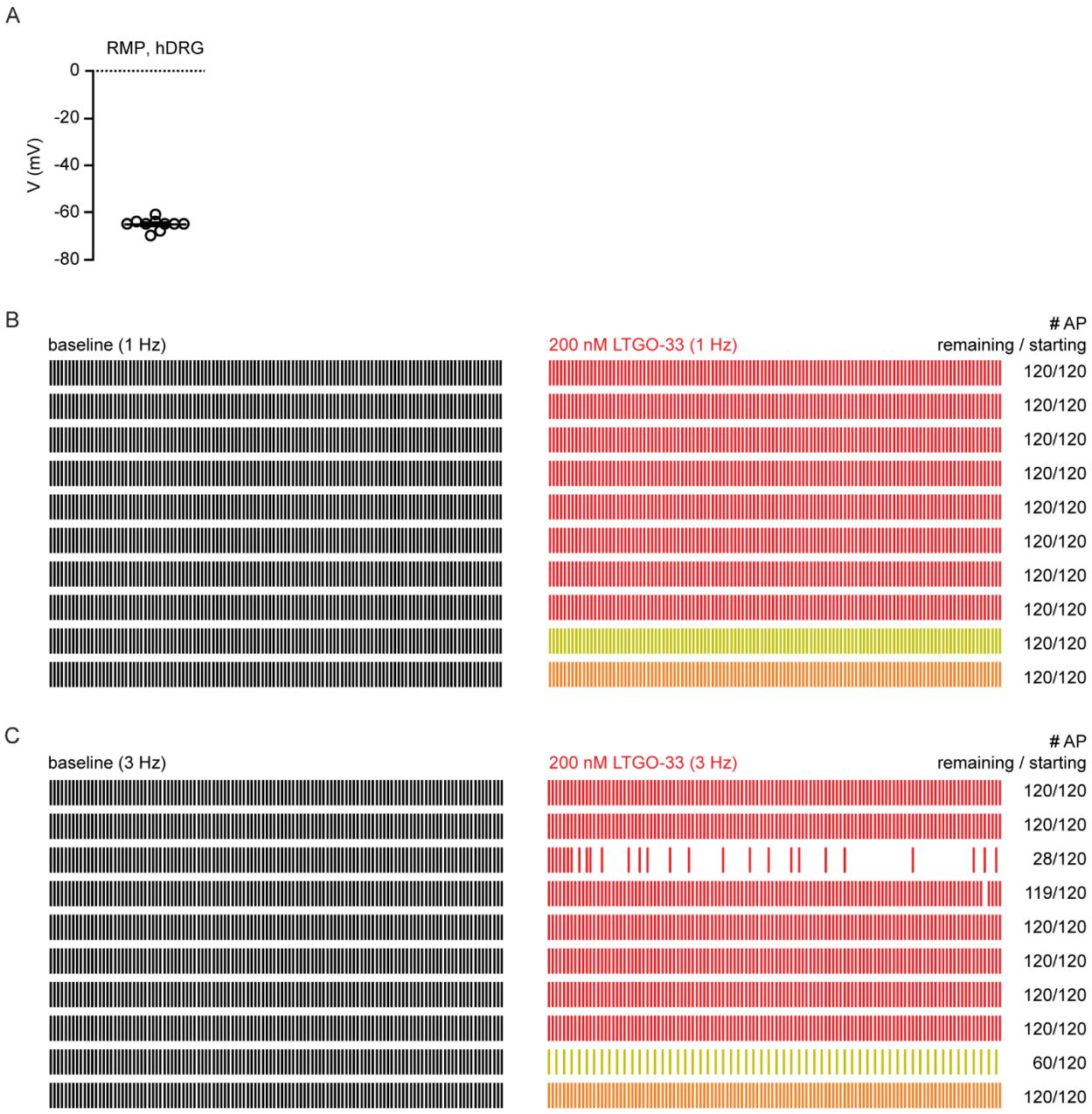

Supplemental Figure 3. Resting membrane potential (RMP) of human DRG neurons used for current clamp studies and raster plots for 1 and 3 Hz stimulation protocols.

A) RMP of hDRG neurons studied in Fig 2. Average RMP is -65 mV ± 2.4 mV. Mean ± SD. n = 10 cells.
B) Raster plot depicting individual APs for hDRG neurons stimulated at 1 Hz for 120 pulses at baseline (black) and after treatment with 200 nM LTGO-33 (red). Orange and mustard lanes indicate specific cells shown in Fig 2.
C) Raster plot depicting individual APs for hDRG neurons stimulated at 3 Hz for 120 pulses at baseline (black) and after treatment with 200 nM LTGO-33 (red). Orange and mustard lanes indicate specific cells shown in Fig 2.

Figure S4

A

$Na_V1.8$ - % identity

rat	100				
mouse	93.92	100			
dog	82.41	81.97	100		
human	83.1	82.25	88.48	100	
cyno	83.46	82.46	88.53	97.65	100
	rat	mouse	dog	human	cyno

B

Na_V VSDII - % identity

$hNa_V1.8$	100									
$hNa_V1.9$	61.95	100								
$rNa_V1.8$	85.09	56.64	100							
$hNa_V1.5$	72.22	62.04	70.37	100						
$hNa_V1.7$	68.52	62.04	64.81	74.07	100					
$hNa_V1.4$	69.44	60.19	67.59	78.7	88.89	100				
$hNa_V1.6$	69.44	61.11	66.67	76.85	87.04	84.26	100			
$hNa_V1.1$	69.44	60.19	69.44	77.78	86.11	90.74	89.81	100		
$hNa_V1.2$	68.52	60.19	67.59	78.7	84.26	87.04	92.59	93.52	100	
$hNa_V1.3$	69.44	61.11	68.52	80.56	84.26	88.89	89.81	91.67	96.3	100
	$hNa_V1.8$	$hNa_V1.9$	$rNa_V1.8$	$hNa_V1.5$	$hNa_V1.7$	$hNa_V1.4$	$hNa_V1.6$	$hNa_V1.1$	$hNa_V1.2$	$hNa_V1.3$

C

Na_V VSDII alignment

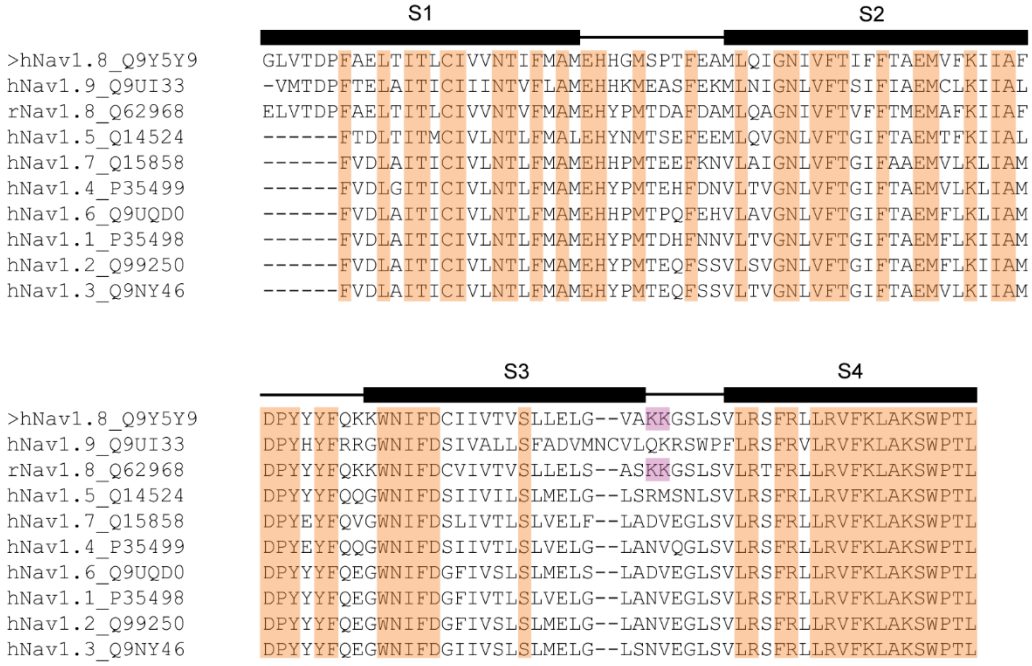

Supplemental Figure 4. Protein identity of hNa_V1.8 across species and sodium channel isoforms.

A) Table of % amino acid identity of $Na_V1.8$ isoforms using the Uniprot sequence for human (*Homo sapiens*, NP_006505.4), cynomolgus monkey (*Macaca fascicularis*, XP_005546741.2), dog (*Canis lupus familiaris*, NP_001003203.1), mouse (*Mus musculus*, NP_033160.2), and rat (*Rattus norvegicus,* NP_058943.2).

B) Table of % amino acid identity of VSDII (S1-S4) using the Uniprot sequence for $hNa_V1.1$ (NP_001159435.1), $hNa_V1.2$ (NP_001035232.1), $hNa_V1.3$ (XP_016860149.1), $hNa_V1.4$ (NP_000325.4, $hNa_V1.5$ (NP_932173.1), $hNa_V1.6$ (NP_055006.1), $hNa_V1.7$ (XP_011509918.1), $hNa_V1.8$ (NP_006505.4), $hNa_V1.9$ (NP_054858.2), and $rNa_V1.8$ (NP_058943.2).

C) Alignment of VSDII (S1-S4) from $hNa_V1.1$-1.9 and $rNa_V1.8$ using the sequences indicated in panel B. Thick black bars above denote transmembrane helices and thin black lines extramembrane linkers. Feature boundaries were adopted from the Uniprot entry for $Na_V1.8$ (Q9Y5Y9). Orange highlighted amino acids are conserved across isoforms. Unique KK sequence in S3-S4 loop is shaded in magenta.

Figure S5

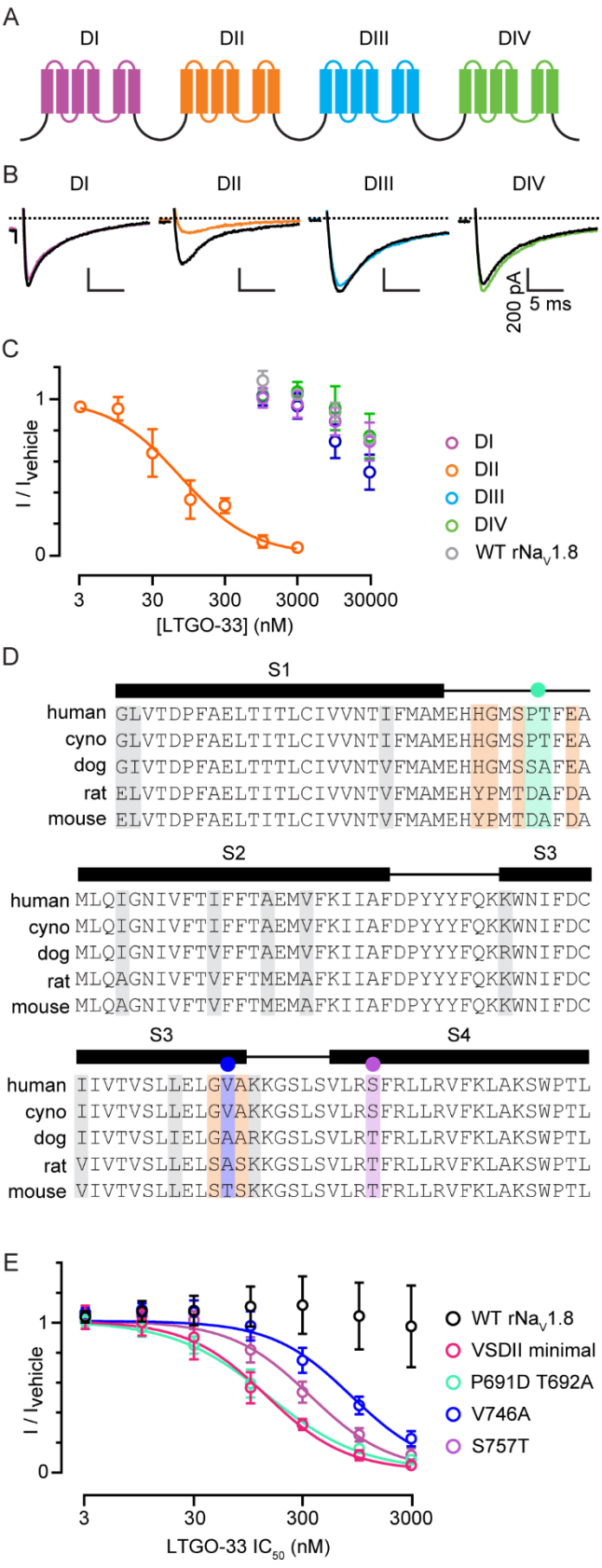

Supplemental Figure 5. Effect of LTGO-33 on human domains (VSD and pore) swapped into rNa$_V$1.8.

A) Schematic depicting the transfer of hNa$_V$1.8 DI-IV (colored) into the rNa$_V$1.8 backbone (black).

B) Example traces of LTGO-33 on Na$_V$1.8 currents in human-rat chimeric channels. Black traces show the currents before and color traces show the currents after LTGO-33 (300 nM for DII, 3 µM for DI, DIII, and DIV,). Scale bars are 5 ms on the horizontal axis and 200 pA on the vertical.

C) Potency of LTGO-33 on WT rNa$_V$1.8 (gray) and human-rat chimeras (color). WT rNa$_V$1.8 data previously shown in Figure 3c. Mean ± SD. n = 6 cells per concentration.

D) Alignment of VSDII for human, cyno, dog, rat, and mouse Na$_V$1.8. Thick black bars above denote transmembrane helices and thin black lines extramembrane linkers. Feature boundaries were adopted from the Uniprot entry for Na$_V$1.8 (Q9Y5Y9). Highlighted amino acids are different between human, dog, rat and/or mouse Na$_V$1.8; gray residues were not changed, orange residues were changed to create the minimal VSDII chimera. Sea foam, blue, and purple dots and shading indicate the sites in the DII minimal chimera that were reverted to the corresponding rat residues.

E) Potency of LTGO-33 on WT rNa$_V$1.8, the VSDII minimal chimera, and three revertant mutants. Mean ± SD. n = 3 cells per concentration for WT rNa$_V$1.8, n = 5 per concentration for VSDII minimal, and n = 4 per concentration for P691D T692A, V746A, and S757T.

Figure S6

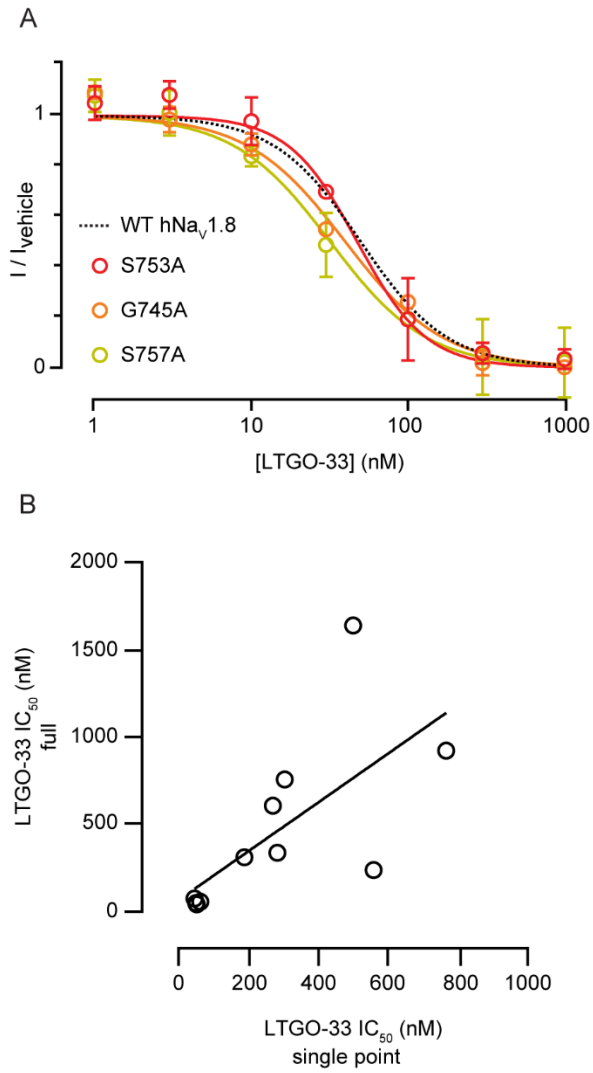

Supplemental Figure 6. LTGO-33 effects on alanine scanning mutagenesis panel.

A) Potency of LTGO-33 on alanine mutants with negligible impact on inhibition but adjacent to residues with 5-fold or greater change in single-point IC_{50}. Dotted black line is WT $hNa_V1.8$ IC_{50} curve from Fig 4d. Mean ± SD. n = 5-6 cells per concentration (Table S6).

B) Comparison of single-point and full IC_{50}s for each mutant where a full IC_{50} was collected. Black line represents a simple linear regression fit (r^2 = 0.46), using the GraphPad Prism function “Simple linear regression”.

Figure S7

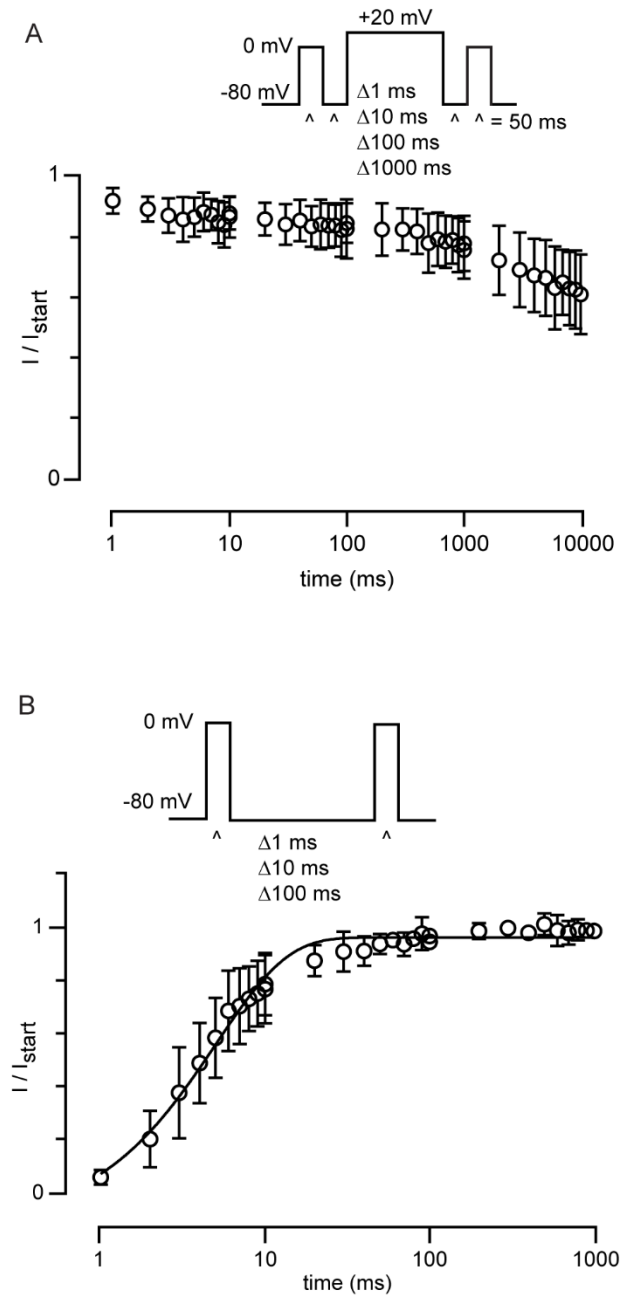

Supplemental Figure 7. Fast and slow inactivation kinetics of hNa$_V$1.8 in HEK293 cells

A) Time-dependence of entry into inactivated state measured using inset voltage protocol. Mean ± SD. n = 6 cells.

B) hNa$_V$1.8 recovery from fast inactivation measured using voltage protocol (top). Mean ± SD. n = 5. Black curve is a single-exponential fit to the average data (tau = 5.1 ms, 95% CI: 4.8 to 5.8 ms, n = 5 cells).

Table S1. hDRG Donor Demographics. Neurons from human DRG donors were used in voltage-clamp and current-clamp studies to measure the activity of LTGO-33 on native channel function.

Donor #	Sex	Age	BMI	Ethnicity	Cause of Death	Displayed in:	Tested at:
1	M	54	31.6	Hispanic	CVA[a]/ICH[b]/Stroke	Figure 1F	Anabios
2	F	48	32	Hispanic	CVA/ICH/Stroke	Figure 1F	Anabios
3	F	32	33.7	Hispanic	Anoxia/Drug Intoxication	Figure 1F	Latigo
4	M	30	25.8	African American	Anoxia/Drug Intoxication	Figure 1F	Latigo
5	M	21	24.4	Caucasian	Head Trauma/Non-MVA[c]	Figure 1F	Latigo
6	F	54	36.1	Hispanic	Anoxia	Figure 2 (LTGO-33)	Anabios
7	F	23	37.8	Caucasian	Anoxia	Figure 2 (LTGO-33)	Anabios
8	M	22	29.2	Hispanic	Head trauma/GSW[d]	Figure 2 (vehicle)	Anabios

[a]Cerebral vascular accident, [b]Intracranial hemorrhage, [c]Motor vehicle accident, [d]Gunshot wound

Table S2. N for each concentration used in IC_{50} measurements in Figure 1d. For IC_{50} measurements where the number of wells, cells, or neurons used was not equal for each concentration, a range of n was provided in the text. For Figure 1d, the specific n per concentration is indicated in the table below.

		n								
	LTGO-33 (nM)	$Na_V1.1$	$Na_V1.2$	$Na_V1.3$	$Na_V1.4$	$Na_V1.5$	$Na_V1.6$	$Na_V1.7$	$Na_V1.8$	$Na_V1.9$
Figure 1d	0.3								7	
	1								6	
	3								7	
	10	4	4	2	4	3	3	6	8	
	30	3	2	4	4	3	2	5	8	
	100	4	4	3	3	4	3	4	7	
	300	4	3	3	3	4	2	7	6	
	1000	3	3	3	4	4	3	6	6	5
	3000	2	4	4	4	4	4	7		4
	10000	4	4	4	4	4	3	7		4
	30000	4	2	2	4	4	2	7		3

Table S3. N for each concentration used in IC_{50} measurements in Figure 1f. For IC_{50} measurements where the number of wells, cells, or neurons used was not equal for each concentration, a range of n was provided in the text. For Figure 1f, the specific n per concentration is indicated in the table below.

		n	
Figure 1f	LTGO-33 (nM)	Human (male)	Human (female)
	3	3	6
	10	3	4
	30	14	6
	100	4	4
	300	15	6
	1000	7	4
	3000	12	6
	10000	5	

Table S4. N for each concentration used in IC_{50} measurements in Figure 4d. For IC_{50} measurements where the number of wells, cells, or neurons used was not equal for each concentration, a range of n was provided in the text. For Figure 4d, the specific n per concentration is indicated in the table below.

		n							
	LTGO-33 (nM)	M682A	L744A	V746A	K749Q	G750A	L752A	R756Q	WT $Na_V1.8$
Figure 4d	1								4
	3								4
	10								4
	30	5	5	6	5	5	5	6	2
	100			5			5	6	3
	300	4	5	6	5	2	5	6	5
	1000		5	5	4	5	5	6	3
	3000	5	5	6	5	5	5	6	2
	10000			5			4	3	
	30000	4	5	1	5	5	3		

Table S5. N for each concentration used in IC_{50} measurements in Figure S2d. For IC_{50} measurements where the number of wells, cells, or neurons used was not equal for each concentration, a range of n was provided in the text. For Figure S2d, the specific n per concentration is indicated in the table below.

		n							
	LTGO-33 (nM)	$Na_V1.1$	$Na_V1.2$	$Na_V1.3$	$Na_V1.4$	$Na_V1.5$	$Na_V1.6$	$Na_V1.7$	$Na_V1.8$
Figure S2d	0.3								8
	1								7
	3								7
	10	4	2	2	2	4	2	6	8
	30	3	4	4	4	4	3	6	8
	100	4	4	4	4	2	3	6	8
	300	2	4	3	4	3	4	5	8
	1000	4	4	3	4	3	4	5	5
	3000	3	4	4	4	4	2	8	
	10000	4	3	3	4	3	3	7	
	30000	3	4	3	2	4	4	5	

Table S6. N for each concentration used in IC_{50} measurements in Figure S6a. For IC_{50} measurements where the number of wells, cells, or neurons used was not equal for each concentration, a range of n was provided in the text. For Figure S6a, the specific n per concentration is indicated in the table below.

		n		
Figure S6a	LTGO-33 (nM)	S753A	G745A	S757A
	1	3	3	3
	3	3	2	2
	10	3	3	3
	30	3	2	2
	100	3	3	3
	300	3	2	2
	1000	6	5	4

Table S7. Boltzmann fit parameters for G-V and SSI relationships of $hNa_V1.8$ stably expressed in HEK293 cells. HEK293 cell stably expressing $hNa_V1.8$ were interrogated with a two-step voltage protocol to measure the G-V and SSI relationships for $hNa_V1.8$. The $V_{1/2}$ and slope were determined using a Boltzmann fit to the normalized data.

Panel	condition	$V_{1/2}$ (mV)	95% CI of $V_{1/2}$ (mV)	Slope	95% CI of slope	n
S1a	HEK293 G-V	8.9 mV	7.5 to 10	8.9	7.8 to 10	10
S1a	HEK293 SSI	-35 mV	-37 to -32	-9.9	-12 to -8.2	10

Table S8. Parameters for rheobase action potentials. For each neuron tested in current-clamp and displayed in Figure 2, the action potential elicited at rheobase (1x) was measured for amplitude, half-width, rheobase, maximum rise slope, and maximum decay slope, both at baseline and after treatment with 200 nM LTGO-33 or vehicle. The mean and SD are plotted for each parameter. Statistical significance was tested with a paired t-test in GraphPad Prism 10.0, with $p < 0.05$ set as the threshold for statistical significance. For half-width and amplitude, the differences (after - before treatment) were compared, and for rheobase, maximum rise slope, and maximum decay slope the ratios (after/before treatment) were compared. N = 10 neurons for 200 nM LTGO-33 treatment and n = 4 for vehicle treatment.

	Baseline		200 nM LTGO-33				
Parameter	Mean	SD	Mean	SD	Mean difference	95% CI	p-value
Half-width	3.8	1.7	4.1	2.4	0.32	-0.70 to 1.3	0.49
Absolute amplitude	120	14	120	15	-0.94	-8.6 to 6.8	0.79
	Mean	SD	Mean	SD	Ratio of means	95% CI	p-value
Rheobase	2000	840	2400	920	1.2	1.1 to 1.3	0.0040
Maximum rise slope	150	63	130	63	0.78	0.66 to 0.93	0.0121
Maximum decay slope	62	18	59	15	0.96	0.88 to 1.0	0.379
	Baseline		Vehicle				
Parameter	Mean	SD	Mean	SD	Mean difference	95% CI	p-value
Half-width	7.0	1.8	7.0	0.60	0.02	-2.0 to 2.0	0.97
Absolute amplitude	140	6.7	130	7.4	-3.5	-10	0.20
	Mean	SD	Mean	SD	Ratio of means	95% CI	p-value
Rheobase	440	420	450	420	1.00	0.90 to 1.2	0.391
Maximum rise slope	120	30	100	40	0.87	0.54 to 1.4	0.42
Maximum decay slope	26	13	34	34	1.1	0.42 to 2.7	0.84

Table S9. Fraction of inhibition by 100 nM LTGO-33 for mutations in hNa$_V$1.8 VSDII and corresponding single-point IC$_{50}$ values. Channels transiently expressed in ND7/23 cells were tested using manual patch clamp electrophysiology. Single-point IC$_{50}$s were fit using a constrained top, bottom, and Hill slope as described in Materials and Methods. Mutants marked with an "X" failed to produce detectable current.

Construct	Fraction current remaining (geo. mean)	Geometric SD factor	IC$_{50}$ (nM; single point)	95% CI (nM)	fold vs WT	n (cells used for IC$_{50}$)
WT	0.29	1.2	43	36 to 49	1.00	14
N678A	0.29	1.2	41	26 to 59	0.96	4
T679A	0.18	1.3	22	14 to 33	0.53	4
I680A	0.42	1.1	75	57 to 96	1.8	5
F681A	X					
M682A	0.74	1.2	290	130 to 1100	6.8	4
M696A	0.28	1.4	42	20 to 72	0.98	5
L697A	0.49	1.4	100	37 to 280	2.4	4
Q698A	0.22	1.2	29	21 to 39	0.69	5
I699A	0.29	1.2	42	28 to 60	1.0	4
G700A	0.24	1.2	32	25 to 4	0.76	5
N701A	0.42	1.1	72	49 to 100	1.7	4
I702A	0.52	1.2	110	69 to 190	2.7	4
V703A	0.33	1.2	50	35 to 69	1.2	4
F704A	0.62	1.3	170	63 to 720	4.1	4
T705A	0.22	1.2	29	20 to 39	0.67	5
V739A	0.55	1.1	120	86 to 180	2.9	4
S740A	0.62	1.3	170	73 to 530	4.0	4
L741A	0.19	1.1	24	20 to 29	0.57	5
L742A	0.32	1.4	50	9 to 140	1.2	3
E743A	X					
L744A	0.89	1.0	770	500 to 1500	18	3
G745A	0.31	1.4	48	10 to 130	1.1	3
V746A	0.85	1.1	570	310 to 1800	13	4
K748A	0.45	1.2	82	53 to 120	1.9	4
K749A	0.48	1.2	95	58 to 150	2.2	4
K749Q	0.73	1.0	270	230 to 320	6.3	4
G750A	0.83	1.2	500	230 to 3500	12	5
S751A	0.54	1.1	120	82 to 170	2.7	4
L752A	0.75	1.1	300	190 to 550	7.1	4
S753A	0.37	1.2	60	23 to 130	1.4	3
V754A	0.35	1.1	54	43 to 68	1.3	3
L755A	0.22	1.1	28	23 to 33	0.66	4
R756A	X					
R756Q	0.63	1.3	190	79 to 610	4.4	5

S757A	0.32	1.1	48	34 to 65	1.1	4
F758A	0.47	1.1	91	74 to 110	2.1	4
R759A	X					
R759Q	0.35	1.1	54	41 to 68	1.3	3
L760A	0.34	1.2	53	32 to 84	1.3	4
L761A	0.38	1.2	61	42 to 86	1.4	4
R762A	0.32	1.0	46	42 to 51	1.1	4
R762Q	0.42	1.2	73	45 to 110	1.7	4
V763A	0.12	1.5	15	8 to 22	0.34	5
F764A	0.33	1.2	51	34 to 73	1.2	4
K765Q	0.12	1.7	16	4 to 30	0.37	4
K765A	0.17	1.7	23	2 to 56	0.55	4
L766A	0.39	1.1	64	49 to 82	1.5	3
K768Q	0.26	1.4	37	14 to 70	0.86	4
K768A	0.2	1.2	26	18 to 35	0.61	4
S769A	0.21	1.2	27	17 to 38	0.63	4
W770A	X					
P771A	0.24	1.3	32	17 to 53	0.76	4

Table S10. LTGO-33 full IC_{50} values for $hNa_V1.8$ VSDII mutations that showed no impact on LTGO-33 inhibition. Channels transiently expressed in ND7/23 cells were tested using manual patch clamp electrophysiology.

Construct	IC_{50} (nM)	95% CI (nM)	n (cells used for IC_{50})
S753A	47	38 to 59	6
G745A	40	34 to 47	5
S757A	32	25 to 41	5